Singular Value Few-shot Adaptation of Vision-Language Models

Taha Koleilat 1* Hassan Rivaz 1 Yiming Xiao 2

¹ Department of Electrical & Computer Engineering, Concordia University, Montreal, Canada ²Department of Computer Science & Software Engineering, Concordia University, Montreal, Canada {taha.koleilat, hassan.rivaz, yiming.xiao}@concordia.ca

Abstract

Vision-language models (VLMs) like CLIP have shown impressive zero-shot and few-shot learning capabilities across diverse applications. However, adapting these models to new fine-grained domains remains difficult due to reliance on prompt engineering and the high cost of full model fine-tuning. Existing adaptation approaches rely on augmented components, such as prompt tokens and adapter modules, which could limit adaptation quality, destabilize the model, and compromise the rich knowledge learned during pretraining. In this work, we present **CLIP-SVD**, a novel multi-modal and parameter-efficient adaptation technique that leverages Singular Value Decomposition (SVD) to modify the internal parameter space of CLIP without injecting additional modules. Specifically, we fine-tune only the singular values of the CLIP parameter matrices to rescale the basis vectors for domain adaptation while retaining the pretrained model. This design enables enhanced adaptation performance using only 0.04% of the model's total parameters and better preservation of its generalization ability. CLIP-SVD achieves state-of-the-art classification results on 11 natural and 10 biomedical datasets, outperforming previous methods in both accuracy and generalization under few-shot settings. Additionally, we leverage a natural language-based approach to analyze the effectiveness and dynamics of the CLIP adaptation to allow interpretability of CLIP-SVD. The code is publicly available at https://github.com/HealthX-Lab/CLIP-SVD.

1 Introduction

Vision-language models (VLMs), such as CLIP [57], have demonstrated remarkable versatility and generalization by aligning images and text through large-scale contrastive pretraining. These models enable powerful zero-shot and few-shot capabilities for various applications, but adapting them effectively to downstream tasks remains non-trivial. Full model fine-tuning is often computationally infeasible, while prompt learning strategies (e.g., CoOp [82] and CoCoOp [81]) may be limited by heavy dependency on handcrafted or learned text prompts. Adapter-based methods, such as CLIP-Adapter [19] and MaPLe [35], infuse additional modules to improve adaptation quality, but this increases model complexity, lowers inference efficiency, and sometimes degrades zero-shot performance by destabilizing pretrained representations [36]. Recent efforts in parameter-efficient fine-tuning (PEFT) aim to overcome these limitations. Among them, Singular Value Fine-Tuning (SVF) [63] has emerged as a compelling strategy by modifying only the singular values of model weight matrices without changing the original model. While SVF has shown promise in CNNs and large language models (LLMs) [63, 49], it has not been fully explored in Transformer-based, multi-modal settings. Furthermore, despite the popularity of CLIP adaptation methods, very few have attempted to interpret the dynamics and effectiveness of model adaptation. Lastly, most CLIP adaptation techniques focus on natural domains alone, with few specialized in biomedical applications

^{*}Coresponding author

Table 1: Natural language-based interpretations for the top 3 Attention Heads associated with the highest normalized changes (sorted in descending order) in the Output-Value circuit after CLIP adaptation for different datasets. Here, "L" denotes layer while "H" denotes attention head.

EuroSAT (Satellite Images)	DTD (Texture Images)
(L10.H0): Aerial Landscapes & Environments (L10.H10): Mood, Atmosphere & Highlights (L11.H0): Semantic Layout & Spatial Context	(L8.H6) Refined Textural Details of Everyday Objects (L10.H2) Cultural & Textural Scenes (L9.H4) Natural Landscapes & Textures
SUN397 (Scene Understanding)	UCF101 (Action Recognition)
(L11.H0): Semantic Layout & Spatial Context (L11.H2): Numbers, Symbols & Temporal Cues (L11.H3): Lifestyle & Tranquil Activities	(L10.H5) Action, Emotion & Faces (L10.H6) Organic Flow & Movement (L10.H1) Human Experiences & Objects in Action
BUSI (Breast Ultrasound)	BTMRI (Brain MRI)
(L11.H8): Converging Edges & Cluster Markers (L8.H6): Contour Irregularity & Internal Spread (L8.H3): Radiologic Artifacts & Diffuse Shapes	(L8.H9) Scattered Highlights & Artifactual Spots (L8.H0) Focal Markers & Shape Cues (L9.H5) Streaks, Texture, & Soft Borders
COVID-QU-Ex (Chest X-ray)	CTKIDNEY (Kidney CT)
(L11.H0): Signal Voids & Shifts (L9.H1): Ring-Like Structures & Localized Spread (L11.H3): Cross-Lobe Flow & Density Buildup	(L8.H6): Contour Irregularity & Internal Spread (L8.H3): Radiologic Artifacts & Diffuse Shapes (L8.H10): Diffuse Zones & Overlapping Shapes

[5, 39] due to distinctive visual features and complex clinical descriptions. This creates a gap for a universal strategy that can generalize effectively across natural and biomedical domains without high computational complexity or tailored adjustments (e.g., specialized prompt engineering [5, 39]). To address the aforementioned challenges, we present CLIP-SVD, a novel parameter-efficient few-shot framework for unified CLIP adaptation across both natural and biomedical domains. While many methods [82] primarily focus on the text branch, recent ones [35] have shown the benefit of adapting image and text branches jointly, at the cost of heavy "add-on" modules. For example, the popular MaPLe requires additional trainable parameters for 2.85% of the CLIP model. In contrast, our approach leverages Singular Value Decomposition (SVD) to decompose the projection weights in CLIP's attention and feedforward layers into corresponding singular values and singular vectors, with only the first fine-tuned for both image and text encoders. We hypothesize that this allows the model to rescale the basis vectors for each downstream task with superior adaptation quality and generalizability. Furthermore, our combination of CLIP's multi-head attention and SVD-based weight adaptation invites an opportunity for a natural language-based paradigm to localize, rank, and semantically "describe" the most significant dynamic shifts in the adapted model. Here, we probe the best text basis to map the semantic meaning of the attention heads [18] with the most significant updates through CLIP-SVD, as shown in Table 1 for 16-shot CLIP adaptation on distinct tasks. Compared with previous efforts [63] that rely on visual interpretation and/or model weight statistics, this approach offers more intuitive and granular insights into CLIP adaptation. Yet, a related text corpus for analyzing biomedical data is still unavailable. Our study has four major contributions: First, we proposed an SVD-based few-shot adaptation framework for Transformer-based multi-modal settings (e.g., CLIP and BiomedCLIP) for the first time, requiring just **0.04**% of the model's total parameters, significantly lower than other multi-modal methods. Second, we performed comprehensive validation with 11 natural and 10 biomedical domain datasets, demonstrating CLIP-SVD's superior performance against the state-of-the-art (SOTA) methods in both accuracy and generalization. Third, with ranked weight changes associated with our method, we adopted a natural language-facilitated approach to intuitively interpret the effectiveness and dynamics of task-specific CLIP adaptation. Lastly, to meet an urgent need for semantic interpretation of attention heads in CLIP for biomedical applications (e.g., analysis of CLIP-SVD), we built the first corpus of biomedical image descriptions.

2 Related Works

2.1 Parameter-efficient Fine-tuning

Fine-tuning large VLMs is often computationally prohibitive for domain-specific adaptation. Parameter-efficient fine-tuning addresses this by updating only a small subset of parameters while keeping the backbone frozen [45]. Selective tuning methods like BitFit [74] adjust only bias terms

while pruning and sparsity techniques can further reduce trainable parameters [21, 25], though they often compromise robustness in zero-shot settings. Adapter-based tuning offers a more robust alternative by inserting lightweight modules [59, 26, 32, 12, 46], but can introduce inference latency [54]. Popular prompt tuning [42, 44, 31] and Low-Rank Adaptation (LoRA) [27] provide other PEFT strategies, with LoRA inserting low-rank matrices to minimize overfitting [43, 2]. However, these methods typically rely on external, randomly initialized modules, risking destabilization and forgetting of original CLIP knowledge [78, 85]. Designing PEFT methods that enhance adaptation without compromising pre-trained strengths remains a major goal. Recently, Singular Value Fine-Tuning (SVF) [63] has emerged as a promising alternative. Initially applied to CNNs for segmentation with strong results, SVF modifies only the singular values of weight matrices while preserving their directions without introducing new modules. Later, SAM-PARSER [53] extended SVF to large vision Transformer models, but limited its application to the vision encoder, without fine-tuning query, key, and value (Q, K, V) matrices crucial for cross-modal tasks. Additionally, SVD-based methods have shown effectiveness in LLMs [49], but their potential for multi-modal VLM adaptation remains largely unexplored, offering an exciting direction for future research.

2.2 Adapting Vision-Language Models

Vision-language models, such as CLIP [57] and ALIGN [30] have significantly advanced multi-modal learning by aligning image and text embeddings in a shared space using self-supervised contrastive training. These models perform well on general-domain tasks like zero-shot classification and cross-modal retrieval, but their reliance on broad, non-specialized datasets limits their effectiveness in expert domains, such as healthcare, where nuanced visual cues and domain-specific semantics are critical. To address this, recent research has explored adapting VLMs to specialized settings using techniques like prompt learning, which offers a lightweight alternative to full fine-tuning. Methods, such as CoOp [82] and CoCoOp [81] learn optimized prompts while keeping the VLM backbone frozen, with extensions like MaPLe [35] and PromptSRC [36] improving robustness through encoder tuning and self-regularization. Adapter-based strategies like CLIP-Adapter [19] and Tip-Adapter[77] modify the visual branch or incorporate support-set features to boost few-shot performance, although they may face optimization hurdles. Enhanced probing methods such as LP++ [28] further refine adaptation by balancing modality-specific features with adaptive learning dynamics. In the biomedical domain, adaptations of CLIP like BioViL [6], PubMedCLIP [16], and BiomedCLIP [79] leverage domain-specific corpora to improve relevance, with specific methods bridging general-purpose biomedical VLMs and specialized clinical tasks [37, 38, 62, 58]. Yet, these models still struggle with fine-grained clinical understanding [70, 80]. Prompt-learning methods, including XCoOp [5] and DCPL[9], extend CoOp-style tuning to medical applications, but often demand relatively large training sets. In comparison, BiomedCoOp [39] demonstrates that prompt tuning can preserve generalization across diverse medical tasks even in low-resource conditions. Despite this broad range of techniques, no method has yet achieved robust performance across both natural and biomedical domains.

3 Method

3.1 CLIP Preliminaries

CLIP consists of a vision encoder E_v and a text encoder E_t that project images and text into a shared embedding space. Given a batch of B images and C distinct classes, image inputs $X_v \in \mathbb{R}^{B \times 3 \times H \times W}$ are RGB images of height H and width W, and text inputs $X_t \in \mathbb{R}^{C \times L}$ are tokenized sequences of length L, where each sequence serves as a text prompt representing a single class.

The encoders generate modality-specific features:

$$\mathbf{V} = \mathbf{E}_{v}(\mathbf{X}_{v}) \in \mathbb{R}^{B \times D}, \quad \mathbf{T} = \mathbf{E}_{t}(\mathbf{X}_{t}) \in \mathbb{R}^{C \times D}$$
 (1)

where D is the embedding dimension and C is the number of candidate classes. Both ${\bf V}$ and ${\bf T}$ are L2-normalized onto the unit hypersphere.

In zero-shot classification, CLIP matches an image to C class descriptions (e.g., "a photo of a [CLASS]"). The probability of assigning image embedding $\hat{\mathbf{V}}$ to class k is:

$$p(Y = k | \hat{\mathbf{V}}, \hat{\mathbf{T}}) = \frac{\exp(\hat{\mathbf{V}}^{\top} \hat{\mathbf{T}}^{(k)} / \tau)}{\sum_{j=1}^{C} \exp(\hat{\mathbf{V}}^{\top} \hat{\mathbf{T}}^{(j)} / \tau)}$$
(2)

where τ is a learnable temperature parameter. The predicted class \hat{k} is:

$$\hat{k} = \arg\max_{k} p(Y = k|\hat{\mathbf{V}}, \hat{\mathbf{T}})$$
(3)

This formulation enables CLIP to generalize to unseen categories by leveraging the alignment between images and natural language descriptions.

3.2 Singular Value Decomposition of Weight Matrices

SVD-Based Decomposition of Pre-trained Weights: The overall framework of CLIP-SVD is shown in Fig. 1. For our proposed CLIP-SVD technique, we decompose the weight matrices in the **Multi-Head Self-Attention (MHSA)** and **Multi-Layer Perceptron (MLP)** blocks of each Transformer layer in CLIP's text and image encoders with SVD. Specifically, each weight matrix W in the MHSA and MLP blocks can be factorized using SVD as follows:

$$W = USR^{\top} \tag{4}$$

where $U \in \mathbb{R}^{d \times r}$ is the left singular vector matrix, $S = diag(\lambda_1, \lambda_2, \lambda_3, ..., \lambda_r) \in \mathbb{R}^{r \times r}$ is a diagonal matrix containing the singular values $(\lambda_1 \geq \lambda_2 \geq \cdots \geq \lambda_r \geq 0)$ arranged in a descending order, $R \in \mathbb{R}^{m \times r}$ is the right singular vector matrix, and $r = \min(d, m)$ is the rank of W. Instead of fully modifying W directly, we **freeze the singular vectors** U and R and **fine-tune only the singular values** λ_i . Note that we adapt the vector of full-rank singular values for our application. We further analyze the effect of different rank configurations in Appendix D.

Multi-Head Self-Attention Computation: Each Transformer layer in CLIP-type models applies MHSA using the Query (Q), Key (K), Value (V), and Output (O) projection matrices:

$$W_Q, W_K, W_V \in \mathbb{R}^{D \times d}, \quad W_O \in \mathbb{R}^{d \times D}.$$
 (5)

Given an input $X \in \mathbb{R}^{B \times L \times D}$, self-attention for the h^{th} head is computed as:

$$Q_h = XW_{Q_h} = X(U_{Q_h}S_{Q_h}R_{Q_h}^{\top}), K_h = XW_{K_h} = X(U_{K_h}S_{K_h}R_{K_h}^{\top})$$
(6)

$$Z_{h} = \operatorname{softmax}\left(\frac{Q_{h}K_{h}^{\top}}{\sqrt{d}}\right)(XW_{V_{h}}) = \operatorname{softmax}\left(\frac{Q_{h}K_{h}^{\top}}{\sqrt{d}}\right)(XU_{V_{h}}S_{V_{h}}R_{V_{h}}^{\top}) \tag{7}$$

where B is the batch size, L is the sequence length, D is the embedding dimension, and d is the dimension of each attention head.

For G attention heads of a Transformer layer:

$$Z_{\text{MHSA}} = \text{Concat}(Z_1, \dots, Z_G)(W_O) = \text{Concat}(Z_1, \dots, Z_G)(U_O S_O R_O^\top). \tag{8}$$

The output of the multi-head self-attention is then combined with the input via a residual connection:

$$X' = X + Z_{\text{MHSA}}. (9)$$

Feed-forward Network: Following the self-attention block, the updated representation X' is passed through a feedforward MLP block ($\{W_{in}, W_{out}\}$), which is also decomposed using SVD. The MLP applies two linear transformations with an activation function in between, and finally, a residual connection is applied:

$$H = \text{ReLU}(X'W_{in}) = \text{ReLU}(X'U_{in}S_{in}R_{in}^{\top})$$
(10)

$$X'' = H(W_{out}) = H(U_{out}S_{out}R_{out}^{\top})$$
(11)

$$X_{\text{out}} = X' + X''. \tag{12}$$

With CLIP-SVD, each Transformer layer maintains its original representational capacity by rescaling the singular vectors, thus allowing robust adaptation and retention of pretrained knowledge.

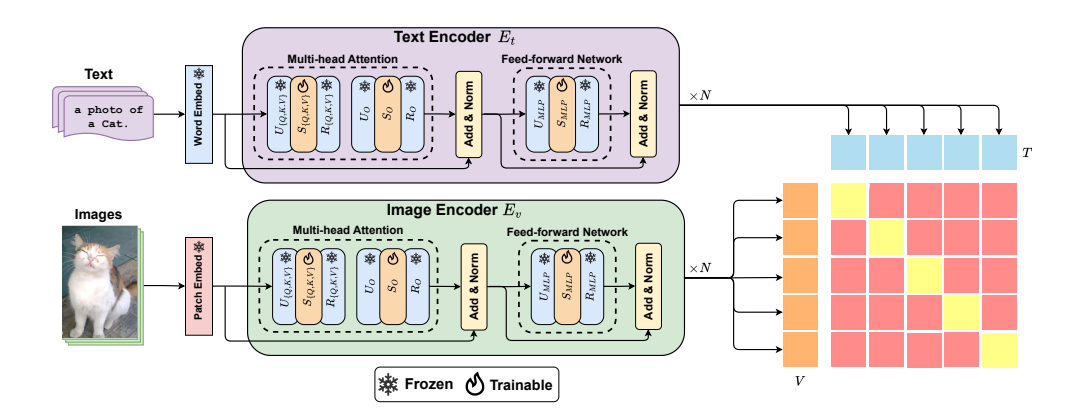


Figure 1: The overall framework of CLIP-SVD. We decompose the Query, Key, Value, and Output projection weights $(W_Q, W_K, W_V \text{ and } W_O)$ of the MHSA blocks in both vision and text encoders E_v and E_t , as well as the linear weights of the Feed-forward Networks (W_{MLP}) in all layers. We finetune only the singular values S of the SVD decomposed weights.

3.3 Interpretation of CLIP-SVD with TextSpan

To understand how our adaptation reshapes CLIP's internal representations, we utilize TextSpan [18], which aligns text descriptions to each attention head h of layer l in the ViT image encoder to reveal their semantic roles. This is achieved by decomposing the MHSA outputs $x^{l,h}$ into a summation of contributions from image tokens through SVD:

$$x^{l,h} = \sum_{i=0}^{N} x_i^{l,h}, \quad x_i^{l,h} = \alpha_i^{l,h} W_O^{l,h} W_V^{l,h} z_i^{l-1} = \alpha_i^{l,h} (U^{l,h} S^{l,h} V^{l,h\top}) z_i^{l-1}, \tag{13}$$

where $\alpha_i^{l,h}$ denotes the attention weight from the class token to token i, and z_i^{l-1} is the input token representation. Text Span interprets the semantic roles of heads by projecting candidate text features $\mathbf{T}_{\text{corpus}}$ into the span of $x^{l,h}$:

$$\tilde{\mathbf{T}}^{l,h} = x^{l,h} (x^{l,h^{\top}} x^{l,h})^{-1} x^{l,h^{\top}} \mathbf{T}_{\text{corpus}}, \text{ with } P^{l,h} = x^{l,h} \cdot \tilde{\mathbf{T}}^{l,h^{\top}}, \tag{14}$$

and identifies directions that maximize explained variance in $P^{l,h}$. Importantly, this procedure depends only on the span of the singular vectors $U^{l,h}$, not their magnitudes. In contrast, CLIP-SVD finetunes only the singular values $S^{l,h}$:

$$\tilde{x}_{i}^{l,h} = \alpha_{i}^{l,h} U^{l,h} \tilde{S}^{l,h} V^{l,h\top} z_{i}^{l-1} = \alpha_{i}^{l,h} \sum_{j} \tilde{s}_{j}^{l,h} \langle v_{j}^{l,h}, z_{i}^{l-1} \rangle u_{j}^{l,h}, \tag{15}$$

which preserves the Output-Value (OV) subspace $\mathrm{span}(U^{l,h})$ while reweighting its basis directions through $\tilde{s}_j^{l,h}$. Thus, $\mathrm{TextSpan}$ and $\mathrm{CLIP}\text{-SVD}$ are complementary: the former reveals which semantic directions are encoded in $\mathrm{span}(U^{l,h})$, while the latter modulates how much each direction contributes after adaptation. To quantify these effects, we rank heads by the normalized change in their singular values $S_O^{l,h}$ and $S_V^{l,h}$, summing absolute changes across both matrices. This provides a direct measure of the functional shifts in heads that $\mathrm{TextSpan}$ already grounds in interpretable text semantics.

4 Experiments and Results

4.1 Benchmark evaluation settings

Few-Shot Learning: To assess the model's performance under limited supervision, we conduct few-shot image classification experiments with varying numbers of labeled examples per class (K = 1, 2, 4, 8, and 16 shots) to assess the robustness of our method across both natural and biomedical

domains. This is critical for evaluating the method's ability to learn effectively from sparse data by obtaining task-specific knowledge while retaining general domain comprehension.

Base-to-Novel Generalization: We evaluate the generalizability of CLIP-SVD in natural and biomedical domains, and follow a zero-shot setting, where the datasets are split into base and novel classes for classification tasks. Here, the model is trained only on the base classes in a few-shot setting and evaluated on both base and novel categories. Additionally, we compute the harmonic mean (HM) of both base and novel class prediction accuracies.

Cross-dataset Evaluation: To validate the performance of our approach in cross-dataset transfer, we evaluate our ImageNet-trained model directly on other datasets in the natural domain. Consistent with previous methods, our model is trained on all 1000 ImageNet classes in a few-shot manner. Due to the lack of a similar ImageNet-like dataset and large domain shifts across datasets, we didn't perform cross-dataset evaluation for the biomedical domain.

Datasets: For the natural domain, we follow [82, 81] and evaluate the performance of our method on 11 image classification datasets that cover a wide range of recognition tasks. This includes two generic-objects datasets, ImageNet [15] and Caltech101 [17]; five fine-grained class-specific datasets, OxfordPets [52], StanfordCars [40], Flowers102 [51], Food101 [8], and FGVCAircraft [48]; a scene recognition dataset SUN397 [69]; an action recognition dataset UCF101 [61]; a texture dataset DTD [13] and a satellite-image dataset EuroSAT [22]. For the biomedical domain, we follow [39] and evaluate the performance of our method on 10 diverse medical imaging datasets covering 9 different organs and 8 imaging modalities: Computerized Tomography (CTKidney [29]), Endoscopy (Kvasir [55]), Fundus Photography (RETINA [56, 41]), Histopathology (LC25000 [7], CHMNIST [33]), brain tumor Magnetic Resonance Imaging (BTMRI [50]), Optical Coherence Tomography (OCTMNIST [34]), breast ultrasound (BUSI [3]), and chest and knee X-Ray (COVID-QU-Ex [64], KneeXray [10]).

Implementation Details We use a few-shot training strategy in all experiments, with random sampling for each class. We use the ViT-B/16 CLIP and BiomedCLIP models for natural and biomedical domains, respectively. All models are trained using a batch size of 32 and the AdamW optimizer[47] with a weight decay of 0.01 on a single NVIDIA A100 GPU (40GB RAM). For natural image datasets, we set the learning rate at 5×10^{-4} for few-shot classification, 6×10^{-4} for base-to-novel evaluations, and 5×10^{-4} for cross-dataset transfer tasks. In the biomedical domain, learning rates are optimized per dataset based on validation performance, depending on task complexity and data modality. We report classification accuracies averaged over three independent runs. Prompt templates and full hyperparameter configurations are detailed in Appendix A and B, respectively.

4.2 Few-shot Evaluation

Our method demonstrates superior performance in few-shot learning across both natural and biomedical domains, as shown in Tables 2 and 3. In the natural domain, CLIP-SVD achieves a +1.00% improvement over the second-best method (CLIP-LoRA) in the 1-shot setting (73.20% vs. 72.20%). In the biomedical domain, it surpasses the second-best approach (BiomedCoOp) by +4.28% in the 8-shot setting (73.24% vs. 68.96%). These consistent gains highlight the robustness and effectiveness of our SVD-based tuning strategy across diverse domains.

4.3 Base-to-Novel Generalization

Our method demonstrates strong base-to-novel generalization across both natural and biomedical domains, as shown in Tables 4 and 5. In the natural domain, CLIP-SVD improves over MaPLe by +1.67% on base accuracy, +1.06% on novel accuracy, and +1.58% on the harmonic mean, despite MaPLe being approximately 38× more computationally expensive. In the biomedical domain, CLIP-SVD achieves substantial gains over BiomedCoOp, improving base accuracy by +4.04%, novel accuracy by +0.41%, and the harmonic mean by +4.21%. These results highlight the robustness and scalability of our SVD-based tuning approach across domains. In addition, they also demonstrate the benefit of multi-modal tuning. The proposed CLIP-SVD enhances generalization without compromising the powerful representations learned during CLIP's pretraining.

Table 2: **Evaluation against state-of-the-art techniques for natural domain:** The average classification accuracy (%) obtained from 11 benchmarks derived from 3 sampled support sets for each dataset. The top-performing results are in bold, and the second-best are underlined.

Method	K = 1	K = 2	K = 4	K = 8	K = 16
Zero-shot CLIP [57]			65.36		
CoOp [82]	68.09	70.13	73.59	76.45	79.01
CoCoOp [81]	66.95	67.63	71.98	72.92	75.02
ProGrad [84]	68.20	71.78	74.21	77.93	79.20
KgCoOp [71]	69.51	71.57	74.48	75.82	77.26
MaPLe [35]	69.27	72.58	75.37	78.89	81.79
Linear Probing [57]	45.77	56.92	66.79	73.43	78.39
LP++ [28]	70.35	72.93	75.77	77.94	80.32
CLIP-Adapter [19]	67.87	70.20	72.65	76.92	79.86
Tip-Adapter [77]	68.89	70.42	72.69	74.41	76.44
Tip-Adapter-F [77]	70.62	73.08	75.75	78.51	81.15
GDA [68]	69.39	73.09	76.24	79.71	81.70
ProKeR [4]	71.32	73.74	76.23	79.84	82.01
AdaLoRA [76]	69.04	72.21	75.50	78.13	80.95
TCP [73]	70.63	73.59	76.07	78.39	80.98
CLIP-LoRA [75]	<u>72.20</u>	<u>75.41</u>	<u>77.32</u>	<u>80.10</u>	82.89
CLIP-SVD (Ours)	73.20	76.06	78.18	80.55	82.97

Table 3: Evaluation against state-of-the-art techniques for biomedical domain: The average classification accuracy (%) obtained from 10 benchmarks derived from 3 sampled support sets for each dataset. The top-performing results are in bold, and the second-best are underlined.

Method	K = 1	K = 2	K = 4	K = 8	K = 16
Zero-shot BiomedCLIP [79]			42.38		
CoOp [82]	52.59	55.71	61.35	67.74	71.48
CoCoOp [81]	50.88	53.91	57.63	63.15	67.51
ProGrad [83]	53.67	56.42	62.10	67.06	69.21
KgCoOp [72]	54.31	55.79	60.92	66.00	67.71
Linear Probing [57]	48.91	55.82	62.12	67.33	70.81
LP++ [28]	49.27	55.88	61.30	65.48	70.09
CLIP-Adapter [19]	45.53	44.70	45.30	46.54	48.46
Tip-Adapter [77]	50.35	53.50	58.33	62.01	67.60
Tip-Adapter-F [77]	52.55	54.17	62.30	68.12	68.12
MaPLe [35]	37.99	40.89	44.09	47.37	52.93
BiomedCoOp [39]	56.87	59.32	64.34	68.96	73.41
CLIP-SVD (Ours)	<u>56.35</u>	62.63	68.02	73.26	76.46

4.4 Cross-dataset Transfer

Table 6 shows that CLIP-SVD achieves the highest average accuracy of 66.99%, slightly outperforming MaPLe's 66.30%. It obtains the best performance on several target datasets, including Aircraft (+1.29%), SUN397 (+0.73%), and UCF101 (+1.22%). These results suggest that CLIP-SVD offers strong cross-dataset transfer capabilities, confirming its potential for effective generalization.

4.5 Ablation Experiments: Selective Model Component Fine-tuning

Effect of Tuning Different Weights: We ablated CLIP-SVD's components $(W_Q, W_K, W_V, W_O,$ and $W_{MLP})$ under a 4-shot setting in natural and biomedical domains (see Table 7). Without adaptation, the accuracy was 65.36% (natural) and 42.38% (biomedical). Adding W_O alone substantially

Table 4: Base-to-novel generalization comparison measured by classification accuracy (%) between CLIP-SVD and SOTA methods on 11 natural domain datasets.

Acc.	CLIP	CoOp	CoCoOp	KgCoOp	ProGrad	MaPLe	IVLP	GDA	TCP	CLIP-LoRA	CLIP-SVD
Base	69.34	82.69	80.47	80.73	82.48	82.28	84.21	83.96	84.13	84.10	84.38
Novel	74.22	63.22	71.69	73.60	70.75	<u>75.14</u>	71.79	74.53	75.36	74.80	76.29
HM	71.70	71.66	75.83	77.00	76.16	78.55	77.51	78.72	79.51	<u>79.18</u>	80.13

Table 5: Base-to-novel generalization comparison measured by classification accuracy (%) between CLIP-SVD and SOTA methods on 10 biomedical domain datasets.

Acc.	BiomedCLIP	CoOp	CoCoOp	KgCoOp	ProGrad	MaPLe	XCoOp	BiomedCoOp	GDA	DCPL	CLIP-LoRA	CLIP-SVD
Base	49.27	76.71	75.52	71.90	75.69	65.40	74.62	78.60		73.70	70.56	82.64
Novel	67.17	65.34	67.74	65.94	67.33	49.51	63.19	73.90		69.35	59.84	74.31
HM	55.23	68.80	69.11	67.22	69.86	53.10	68.43	74.04		71.46	64.76	78.25

Table 6: Cross-dataset natural image benchmark with classification accuracy (%)

	Source		Target									
	ImageNet	Caltech 101	OxfordPet	Stanford Cars	Flowers102	Foodloi	Aircraft	SUR391	DID	Furo SAI	UCFIOI	Average
CLIP	66.72	92.98	89.13	65.29	71.30	86.11	24.90	62.59	44.56	47.84	66.83	65.15
CoOp	71.51	93.70	89.14	64.51	68.71	85.30	18.47	64.15	41.92	46.39	66.55	63.88
Co-CoOp	71.02	94.43	90.14	65.32	71.88	86.06	22.94	67.36	45.73	45.37	68.21	65.74
KgCoOp	70.66	93.92	89.83	65.41	70.01	86.36	22.51	66.16	46.35	46.04	68.50	65.51
ProGrad	72.24	91.52	89.64	62.39	67.87	85.40	20.61	62.47	39.42	43.46	64.29	62.71
MaPLe	70.72	93.53	90.49	65.57	<u>72.23</u>	86.20	24.74	67.01	46.49	48.06	<u>68.69</u>	<u>66.30</u>
CLIP-SVD	<u>72.15</u>	93.68	91.06	65.00	72.45	86.21	26.03	67.74	45.15	47.51	69.91	66.99

improved performance (75.45% and 62.27%), highlighting its importance. Including W_{MLP} further boosted accuracy (77.78% and 66.40%), showing its role in fine-grained transformation. Adding W_Q, W_K , or W_V individually on top of W_O and W_{MLP} led to near-identical results in the natural domain, but slight gains in biomedical, up to 67.40% with W_V . Using all components yielded the best performance (natural: 78.18% and biomedical: 68.02%), confirming the benefit of full adaptation.

Effect of Tuning Image and Text Encoders: trates how different input modality tuning setups affect classification accuracy. Multi-modal tuning (text+image) consistently outperforms unimodal cases in both domains. In the natural domain, text-only and image-only achieve 75.78% and 74.31% accuracy, while their combination reaches 78.18%. In the biomedical domain, multi-modal tuning yields 68.02%, compared to 64.21% (text) and 65.94% (image), suggesting the complementary nature of visual and textual cues, especially valuable in biomedical settings with limited data and higher complexity.

Effect of Tuning Different Layers: The left panel of Fig. 2 shows how freezing different sets of Transformer layers that are matched in both text and image encoders during SVD-based adaptation affects few-shot accuracy in natural and biomedical domains. In the natural domain, accuracy stays relatively stable, dropping only slightly from 78.18% (all layers adapted) to 77.35% (first four layers

Table 7: Impact of each component of the proposed CLIP-SVD on the 4-shot accuracy (%) of natural and biomedical domain benchmarks

The right panel of Fig. 2 illus-

W_Q	W_K	W_V	W_O	W_{MLP}	Natural	Biomedical
×	Х	Х	Х	Х	65.36	42.38
X	X	X	X	✓	76.69	65.27
X	X	X	1	X	75.45	62.27
X	Х	X	1	✓	77.78	66.40
1	1	1	X	X	77.15	65.35
1	1	1	Х	✓	77.83	67.50
1	1	1	1	X	77.88	66.74
1	X	X	1	✓	78.12	66.99
X	1	X	1	✓	78.12	67.09
X	X	1	1	✓	78.11	67.40
✓	✓	✓	✓	✓	78.18	68.02

frozen) and 75.36% (first and last four frozen), suggesting robust, distributed representations. In contrast, the biomedical domain is more sensitive: accuracy drops from 68.02% (all layers adapted)

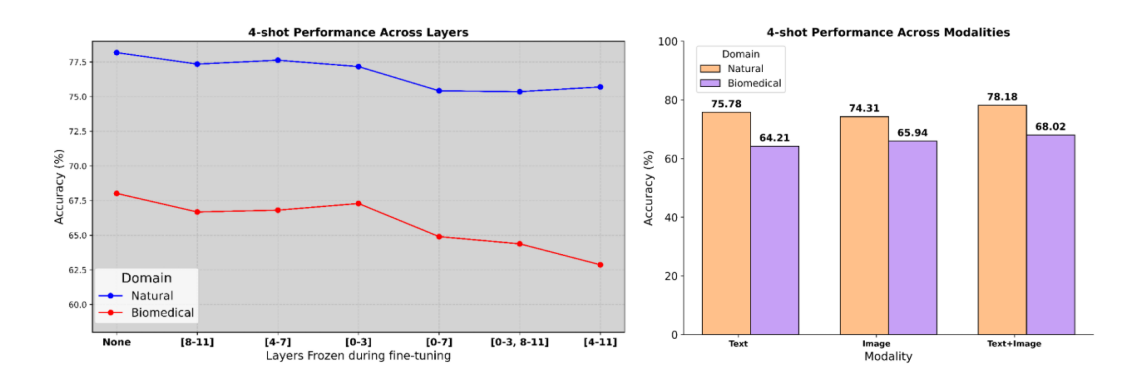


Figure 2: 4-shot performance by freezing certain layers during finetuning (*left*) and by adapting text encoder and/or image encoder (*right*) for natural and biomedical domains.

Table 8: Top 3 descriptions returned by TextSpan [18] applied to the attention head with the greatest adaptation-related change for different datasets.

EuroSAT (L10.H0)	BUSI (L11.H8)	DTD (L8.H6)	
Aerial view of an agricultural field Image taken in the Namibian desert Picture taken in the Brazilian rainforest	A low-contrast region in a clustered pattern A double-density sign suggesting benignity A solid-cystic component suggesting malignancy	Collage of textures Close-up of a textured bark Mesmerizing kinetic sculpture	
BTMRI (L8.H9)	SUN397 (L11.H0)	COVID-QU-Ex (L11.H0)	
An area with decreased perfusion in the left hemisphere A bright spot artifact in a clustered pattern A contrast-enhanced region on axial view	Mysterious day scene Urban rooftop panorama A zoomed out photo	A collapsed lung lobe A low signal-to-noise ratio in the upper lobe A lesion crossing compartments	
UCF101 (L10.H5)	CTKIDNEY (L8.H6)	RETINA (L8.H4)	
Dynamic action Energetic children Playful winking facial expression	An anatomical displacement A spiculated margin A zone of tissue infiltration	An area with decreased perfusion A vascular displacement A vascular structure with sharp borders	

to 66.68% (last four frozen), 64.38% (first and last four), and 62.87% (top eight frozen), indicating that deeper layers are more critical for capturing domain-specific complexity.

4.6 Natural Language-based Interpretation of CLIP-SVD

Natural language offers a powerful but under-explored lens into the conceptual space of VLMs. To gain insights into the impact of CLIP-SVD, we investigate how textual descriptions align with CLIP's internal representations. Besides the natural domain, we present the first systematic, text-based analysis of a biomedical VLM at the attention head level, focusing on how fine-tuning, such as in BiomedCLIP, reshapes semantic VLM's representations. To support this, similar to [18], we constructed a new biomedical caption corpus of 300 clinically relevant text elements using GPT-4 [1], describing features like contrast, shape, and texture. This enables interpretable alignment between vision and language representations and domain-targeted probing of attention heads. Our framework combines CLIP-SVD with TextSpan [18] to quantify semantic shifts in Output-Value circuits of ViT backbones, focusing on the last four layers [18]. By ranking the attention heads via singular value shift magnitude from CLIP-SVD and extracting aligned text spans, we gain an intuitive interpretation for the importance of different attention heads during model adaptation and their roles in the finetuned tasks (see Tables 1 and 8). These analyses highlight how finetuning steers VLMs toward task-relevant, domain-specific understanding. Additionally, the insights could allow debugging and further refinement (e.g., with prompt engineering) of task/domain-specific CLIP models.

5 Limitations

We adopted a natural language-based technique to understand the impact and insights of CLIP-SVD in model adaptation. For the related analyses in the biomedical domain, we constructed a new corpus of biomedical image descriptions by leveraging the large language models. Although it is shown to

facilitate the interpretation, further validation is still required in broader applications, particularly with domain experts. We will investigate this in the near future.

6 Conclusion

In conclusion, we introduced CLIP-SVD, a novel parameter-efficient adaptation method for CLIP models that finetunes only the singular values of the weight matrices while preserving its pre-trained structure. Our approach enables effective few-shot learning with minimal computational overhead, achieving state-of-the-art results across both natural and biomedical domains. Through extensive ablation studies, we demonstrated the critical role of singular value adaptation in enhancing task-specific feature extraction. Further analyses of the Output-Value circuit with a natural-language-based approach revealed that adapting singular values steers attention heads toward more specialized roles, thus opening doors for further investigation of CLIP's characteristics in broader applications.

Acknowledgments and Disclosure of Funding

We acknowledge the support of the Natural Sciences and Engineering Research Council of Canada (NSERC) and the Fonds de recherche du Québec – Nature et technologies (B2X-363874).

References

- [1] Josh Achiam, Steven Adler, Sandhini Agarwal, Lama Ahmad, Ilge Akkaya, Florencia Leoni Aleman, Diogo Almeida, Janko Altenschmidt, Sam Altman, Shyamal Anadkat, et al. Gpt-4 technical report. *arXiv* preprint arXiv:2303.08774, 2023. 9, 19
- [2] Armen Aghajanyan, Sonal Gupta, and Luke Zettlemoyer. Intrinsic dimensionality explains the effectiveness of language model fine-tuning. In *Proceedings of the 59th Annual Meeting of the Association for Computational Linguistics and the 11th International Joint Conference on Natural Language Processing (Volume 1: Long Papers)*, pages 7319–7328, 2021. 3
- [3] Walid Al-Dhabyani, Mohammed Gomaa, Hussien Khaled, and Aly Fahmy. Dataset of breast ultrasound images. *Data in brief*, 28:104863, 2020. 6, 16, 18
- [4] Yassir Bendou, Amine Ouasfi, Vincent Gripon, and Adnane Boukhayma. Proker: A kernel perspective on few-shot adaptation of large vision-language models. In *Proceedings of the Computer Vision and Pattern Recognition Conference*, pages 25092–25102, 2025.
- [5] Yequan Bie, Luyang Luo, Zhixuan Chen, and Hao Chen. Xcoop: Explainable prompt learning for computer-aided diagnosis via concept-guided context optimization. In *International Conference on Medical Image Computing and Computer-Assisted Intervention*, pages 773–783. Springer, 2024. 2, 3
- [6] Benedikt Boecking, Naoto Usuyama, Shruthi Bannur, Daniel C Castro, Anton Schwaighofer, Stephanie Hyland, Maria Wetscherek, Tristan Naumann, Aditya Nori, Javier Alvarez-Valle, et al. Making the most of text semantics to improve biomedical vision–language processing. In *European conference on computer vision*, pages 1–21. Springer, 2022. 3
- [7] Andrew A. Borkowski, Marilyn M. Bui, L. Brannon Thomas, Catherine P. Wilson, Lauren A. DeLand, and Stephen M. Mastorides. Lung and colon cancer histopathological image dataset (lc25000), 2019. 6, 16, 18
- [8] Lukas Bossard, Matthieu Guillaumin, and Luc Van Gool. Food-101–mining discriminative components with random forests. In *ECCV*, pages 446–461. Springer, 2014. 6, 16
- [9] Qinglong Cao, Zhengqin Xu, Yuntian Chen, Chao Ma, and Xiaokang Yang. Domain-controlled prompt learning. In *Proceedings of the AAAI Conference on Artificial Intelligence*, pages 936–944, 2024. 3
- [10] Pingjun Chen. Knee osteoarthritis severity grading dataset, 2018. 6, 16, 18
- [11] Peijie Chen, Qi Li, Saad Biaz, Trung Bui, and Anh Nguyen. gscorecam: What objects is clip looking at? In *Proceedings of the Asian Conference on Computer Vision*, pages 1959–1975, 2022. 21
- [12] Shoufa Chen, Chongjian Ge, Zhan Tong, Jiangliu Wang, Yibing Song, Jue Wang, and Ping Luo. Adaptformer: Adapting vision transformers for scalable visual recognition. *Advances in Neural Information Processing Systems*, 35:16664–16678, 2022. 3
- [13] Mircea Cimpoi, Subhransu Maji, Iasonas Kokkinos, Sammy Mohamed, and Andrea Vedaldi. Describing textures in the wild. In CVPR, pages 3606–3613, 2014. 6, 16
- [14] Noel Codella, Veronica Rotemberg, Philipp Tschandl, M Emre Celebi, Stephen Dusza, David Gutman, Brian Helba, Aadi Kalloo, Konstantinos Liopyris, Michael Marchetti, et al. Skin lesion analysis toward melanoma detection 2018: A challenge hosted by the international skin imaging collaboration (isic). arXiv preprint arXiv:1902.03368, 2019. 16
- [15] Jia Deng, Wei Dong, Richard Socher, Li-Jia Li, Kai Li, and Li Fei-Fei. Imagenet: A large-scale hierarchical image database. In CVPR, pages 248–255. Ieee, 2009. 6, 16, 18
- [16] Sedigheh Eslami, Gerard de Melo, and Christoph Meinel. Does clip benefit visual question answering in the medical domain as much as it does in the general domain?, 2021. 3
- [17] Li Fei-Fei, Rob Fergus, and Pietro Perona. Learning generative visual models from few training examples: An incremental bayesian approach tested on 101 object categories. In CVPR Workshop, pages 178–178. IEEE, 2004. 6, 16

- [18] Yossi Gandelsman, Alexei A Efros, and Jacob Steinhardt. Interpreting clip's image representation via text-based decomposition. *arXiv* preprint arXiv:2310.05916, 2023. 2, 5, 9, 18, 19, 21, 22, 23, 24, 25
- [19] Peng Gao, Shijie Geng, Renrui Zhang, Teli Ma, Rongyao Fang, Yongfeng Zhang, Hongsheng Li, and Yu Qiao. Clip-adapter: Better vision-language models with feature adapters. *International Journal of Computer Vision*, 132(2):581–595, 2024. 1, 3, 7, 19
- [20] Matthieu Guillaumin, Daniel Küttel, and Vittorio Ferrari. Imagenet auto-annotation with segmentation propagation. *International Journal of Computer Vision*, 110(3):328–348, 2014. 21
- [21] Demi Guo, Alexander M Rush, and Yoon Kim. Parameter-efficient transfer learning with diff pruning. In *Proceedings of the 59th Annual Meeting of the Association for Computational Linguistics and the 11th International Joint Conference on Natural Language Processing (Volume 1: Long Papers)*, pages 4884–4896, 2021. 3
- [22] Patrick Helber, Benjamin Bischke, Andreas Dengel, and Damian Borth. Eurosat: A novel dataset and deep learning benchmark for land use and land cover classification. J-STARS, 12(7):2217–2226, 2019. 6, 16
- [23] Dan Hendrycks, Steven Basart, Norman Mu, Saurav Kadavath, Frank Wang, Evan Dorundo, Rahul Desai, Tyler Zhu, Samyak Parajuli, Mike Guo, et al. The many faces of robustness: A critical analysis of out-of-distribution generalization. In ICCV, pages 8340–8349, 2021. 16
- [24] Dan Hendrycks, Kevin Zhao, Steven Basart, Jacob Steinhardt, and Dawn Song. Natural adversarial examples. In *CVPR*, pages 15262–15271, 2021. 16
- [25] Connor Holmes, Minjia Zhang, Yuxiong He, and Bo Wu. Nxmtransformer: semi-structured sparsification for natural language understanding via admm. Advances in neural information processing systems, 34: 1818–1830, 2021. 3
- [26] Neil Houlsby, Andrei Giurgiu, Stanislaw Jastrzebski, Bruna Morrone, Quentin De Laroussilhe, Andrea Gesmundo, Mona Attariyan, and Sylvain Gelly. Parameter-efficient transfer learning for nlp. In *International conference on machine learning*, pages 2790–2799. PMLR, 2019. 3
- [27] Edward J Hu, Phillip Wallis, Zeyuan Allen-Zhu, Yuanzhi Li, Shean Wang, Lu Wang, Weizhu Chen, et al. Lora: Low-rank adaptation of large language models. In *International Conference on Learning Representations*, 2021. 3
- [28] Yunshi Huang, Fereshteh Shakeri, Jose Dolz, Malik Boudiaf, Houda Bahig, and Ismail Ben Ayed. Lp++: A surprisingly strong linear probe for few-shot clip. In *Proceedings of the IEEE/CVF Conference on Computer Vision and Pattern Recognition*, pages 23773–23782, 2024. 3, 7
- [29] Md Nazmul Islam, Mehedi Hasan, Md Kabir Hossain, Md Golam Rabiul Alam, Md Zia Uddin, and Ahmet Soylu. Vision transformer and explainable transfer learning models for auto detection of kidney cyst, stone and tumor from ct-radiography. Scientific Reports, 12(1):1–14, 2022. 6, 16, 18
- [30] Chao Jia, Yinfei Yang, Ye Xia, Yi-Ting Chen, Zarana Parekh, Hieu Pham, Quoc Le, Yun-Hsuan Sung, Zhen Li, and Tom Duerig. Scaling up visual and vision-language representation learning with noisy text supervision. In *International conference on machine learning*, pages 4904–4916. PMLR, 2021. 3
- [31] Menglin Jia, Luming Tang, Bor-Chun Chen, Claire Cardie, Serge Belongie, Bharath Hariharan, and Ser-Nam Lim. Visual prompt tuning. In *European Conference on Computer Vision*, pages 709–727. Springer, 2022. 3
- [32] Rabeeh Karimi Mahabadi, James Henderson, and Sebastian Ruder. Compacter: Efficient low-rank hypercomplex adapter layers. In Advances in Neural Information Processing Systems, pages 1022–1035. Curran Associates, Inc., 2021. 3
- [33] Jakob Nikolas Kather, Cleo-Aron Weis, Francesco Bianconi, Susanne M Melchers, Lothar R Schad, Timo Gaiser, Alexander Marx, and Frank Gerrit Zöllner. Multi-class texture analysis in colorectal cancer histology. *Scientific reports*, 6(1):1–11, 2016. 6, 16, 18
- [34] Daniel S. Kermany, Michael Goldbaum, et al. Identifying medical diagnoses and treatable diseases by image-based deep learning. Cell, 172(5):1122 – 1131.e9, 2018. 6, 16, 18
- [35] Muhammad Uzair Khattak, Hanoona Rasheed, Muhammad Maaz, Salman Khan, and Fahad Shahbaz Khan. Maple: Multi-modal prompt learning. In *Proceedings of the IEEE/CVF Conference on Computer Vision and Pattern Recognition*, pages 19113–19122, 2023. 1, 2, 3, 7, 19, 32, 33

- [36] Muhammad Uzair Khattak, Syed Talal Wasim, Muzammal Naseer, Salman Khan, Ming-Hsuan Yang, and Fahad Shahbaz Khan. Self-regulating prompts: Foundational model adaptation without forgetting. In Proceedings of the IEEE/CVF International Conference on Computer Vision, pages 15190–15200, 2023. 1,
- [37] Taha Koleilat, Hojat Asgariandehkordi, Hassan Rivaz, and Yiming Xiao. Medclip-sam: Bridging text and image towards universal medical image segmentation. In *International Conference on Medical Image Computing and Computer-Assisted Intervention*, pages 643–653. Springer, 2024. 3
- [38] Taha Koleilat, Hojat Asgariandehkordi, Hassan Rivaz, and Yiming Xiao. Medclip-samv2: Towards universal text-driven medical image segmentation. *Medical Image Analysis*, page 103749, 2025. 3
- [39] Taha Koleilat, Hojat Asgariandehkordi, Hassan Rivaz, and Yiming Xiao. Biomedcoop: Learning to prompt for biomedical vision-language models. In *Proceedings of the Computer Vision and Pattern Recognition Conference*, pages 14766–14776, 2025. 2, 3, 6, 7, 16, 33
- [40] Jonathan Krause, Michael Stark, Jia Deng, and Li Fei-Fei. 3d object representations for fine-grained categorization. In *ICCV*, pages 554–561, 2013. 6, 16
- [41] Thomas Köhler, Attila Budai, Martin Kraus, Jan Odstrcilik, Georg Michelson, and Joachim Hornegger. Automatic no-reference quality assessment for retinal fundus images using vessel segmentation, 2013. 6, 16, 18
- [42] Brian Lester, Rami Al-Rfou, and Noah Constant. The power of scale for parameter-efficient prompt tuning. arXiv preprint arXiv:2104.08691, 2021. 3
- [43] Chunyuan Li, Heerad Farkhoor, Rosanne Liu, and Jason Yosinski. Measuring the intrinsic dimension of objective landscapes. In *International Conference on Learning Representations*, 2018. 3
- [44] Xiang Lisa Li and Percy Liang. Prefix-tuning: Optimizing continuous prompts for generation. In Proceedings of the 59th Annual Meeting of the Association for Computational Linguistics and the 11th International Joint Conference on Natural Language Processing (Volume 1: Long Papers), pages 4582– 4597, 2021. 3
- [45] Vladislav Lialin, Vijeta Deshpande, and Anna Rumshisky. Scaling down to scale up: A guide to parameter-efficient fine-tuning. arXiv preprint arXiv:2303.15647, 2023. 2
- [46] Dongze Lian, Daquan Zhou, Jiashi Feng, and Xinchao Wang. Scaling & shifting your features: A new baseline for efficient model tuning. Advances in Neural Information Processing Systems, 35:109–123, 2022. 3
- [47] Ilya Loshchilov and Frank Hutter. Decoupled weight decay regularization. arXiv preprint arXiv:1711.05101, 2017. 6
- [48] Subhransu Maji, Esa Rahtu, Juho Kannala, Matthew Blaschko, and Andrea Vedaldi. Fine-grained visual classification of aircraft. arXiv preprint arXiv:1306.5151, 2013. 6, 16
- [49] Fanxu Meng, Zhaohui Wang, and Muhan Zhang. Pissa: Principal singular values and singular vectors adaptation of large language models. Advances in Neural Information Processing Systems, 37:121038– 121072, 2024. 1, 3
- [50] Msoud Nickparvar. Brain tumor mri dataset, 2021. 6, 16, 18
- [51] Maria-Elena Nilsback and Andrew Zisserman. Automated flower classification over a large number of classes. In *ICVGIP*, pages 722–729. IEEE, 2008. 6, 16
- [52] Omkar M Parkhi, Andrea Vedaldi, Andrew Zisserman, and CV Jawahar. Cats and dogs. In CVPR, pages 3498–3505. IEEE, 2012. 6, 16
- [53] Zelin Peng, Zhengqin Xu, Zhilin Zeng, Xiaokang Yang, and Wei Shen. Sam-parser: Fine-tuning sam efficiently by parameter space reconstruction. In *Proceedings of the AAAI Conference on Artificial Intelligence*, pages 4515–4523, 2024. 3
- [54] Jonas Pfeiffer, Aishwarya Kamath, Andreas Rücklé, Kyunghyun Cho, and Iryna Gurevych. Adapterfusion: Non-destructive task composition for transfer learning. In *Proceedings of the 16th Conference of the European Chapter of the Association for Computational Linguistics: Main Volume*, pages 487–503, 2021.

- [55] Konstantin Pogorelov, Kristin Ranheim Randel, Carsten Griwodz, Sigrun Losada Eskeland, Thomas de Lange, Dag Johansen, Concetto Spampinato, Duc-Tien Dang-Nguyen, Mathias Lux, Peter Thelin Schmidt, Michael Riegler, and Pål Halvorsen. Kvasir: A multi-class image dataset for computer aided gastrointestinal disease detection. In *Proceedings of the 8th ACM on Multimedia Systems Conference*, pages 164–169, New York, NY, USA, 2017. ACM. 6, 16, 18
- [56] Prasanna Porwal, Samiksha Pachade, Ravi Kamble, Manesh Kokare, Girish Deshmukh, Vivek Sahasrabud-dhe, and Fabrice Meriaudeau. Indian diabetic retinopathy image dataset (idrid), 2018. 6, 16, 18
- [57] Alec Radford, Jong Wook Kim, Chris Hallacy, Aditya Ramesh, Gabriel Goh, Sandhini Agarwal, Girish Sastry, Amanda Askell, Pamela Mishkin, Jack Clark, et al. Learning transferable visual models from natural language supervision. In *International conference on machine learning*, pages 8748–8763. PMLR, 2021. 1, 3, 7, 19, 32, 33
- [58] Hamza Rasaee, Taha Koleilat, and Hassan Rivaz. Groundingdino-us-sam: Text-prompted multi-organ segmentation in ultrasound with lora-tuned vision-language models. arXiv preprint arXiv:2506.23903, 2025. 3
- [59] Sylvestre-Alvise Rebuffi, Hakan Bilen, and Andrea Vedaldi. Learning multiple visual domains with residual adapters. *Advances in neural information processing systems*, 30, 2017. 3
- [60] Benjamin Recht, Rebecca Roelofs, Ludwig Schmidt, and Vaishaal Shankar. Do imagenet classifiers generalize to imagenet? In ICML, pages 5389–5400. PMLR, 2019. 16
- [61] Khurram Soomro, Amir Roshan Zamir, and Mubarak Shah. Ucf101: A dataset of 101 human actions classes from videos in the wild. *arXiv preprint arXiv:1212.0402*, 2012. 6, 16
- [62] Pascal Spiegler, Taha Koleilat, Arash Harirpoush, Corey S Miller, Hassan Rivaz, Marta Kersten-Oertel, and Yiming Xiao. Textsam-eus: Text prompt learning for sam to accurately segment pancreatic tumor in endoscopic ultrasound. arXiv preprint arXiv:2507.18082, 2025. 3
- [63] Yanpeng Sun, Qiang Chen, Xiangyu He, Jian Wang, Haocheng Feng, Junyu Han, Errui Ding, Jian Cheng, Zechao Li, and Jingdong Wang. Singular value fine-tuning: Few-shot segmentation requires few-parameters fine-tuning. Advances in neural information processing systems, 35:37484–37496, 2022. 1, 2, 3
- [64] Anas M. Tahir, Muhammad E.H. Chowdhury, Amith Khandakar, Tawsifur Rahman, Yazan Qiblawey, Uzair Khurshid, Serkan Kiranyaz, Nabil Ibtehaz, M. Sohel Rahman, Somaya Al-Maadeed, Sakib Mahmud, Maymouna Ezeddin, Khaled Hameed, and Tahir Hamid. Covid-19 infection localization and severity grading from chest x-ray images. Computers in Biology and Medicine, 139:105002, 2021. 6, 16, 18
- [65] Philipp Tschandl, Cliff Rosendahl, and Harald Kittler. The ham10000 dataset, a large collection of multi-source dermatoscopic images of common pigmented skin lesions. *Scientific data*, page 180161, 2018.
- [66] Laurens van der Maaten and Geoffrey Hinton. Visualizing data using t-sne. *Journal of Machine Learning Research*, 9(86):2579–2605, 2008. 19
- [67] Haohan Wang, Songwei Ge, Zachary Lipton, and Eric P Xing. Learning robust global representations by penalizing local predictive power. In *NeurIPS*, 2019. 16
- [68] Zhengbo Wang, Jian Liang, Lijun Sheng, Ran He, Zilei Wang, and Tieniu Tan. A hard-to-beat baseline for training-free clip-based adaptation. arXiv preprint arXiv:2402.04087, 2024.
- [69] Jianxiong Xiao, James Hays, Krista A Ehinger, Aude Oliva, and Antonio Torralba. Sun database: Large-scale scene recognition from abbey to zoo. In CVPR, pages 3485–3492. IEEE, 2010. 6, 16
- [70] Yan Xu, Rixiang Quan, Weiting Xu, Yi Huang, Xiaolong Chen, and Fengyuan Liu. Advances in medical image segmentation: A comprehensive review of traditional, deep learning and hybrid approaches. *Bioengineering*, 11(10):1034, 2024. 3
- [71] Hantao Yao, Rui Zhang, and Changsheng Xu. Visual-language prompt tuning with knowledge-guided context optimization, 2023. 7, 19, 32, 33
- [72] Hantao Yao, Rui Zhang, and Changsheng Xu. Visual-language prompt tuning with knowledge-guided context optimization. In *Proceedings of the IEEE/CVF conference on computer vision and pattern* recognition, pages 6757–6767, 2023. 7
- [73] Hantao Yao, Rui Zhang, and Changsheng Xu. Tcp: Textual-based class-aware prompt tuning for visual-language model. In *Proceedings of the IEEE/CVF Conference on Computer Vision and Pattern Recognition*, pages 23438–23448, 2024. 7

- [74] Elad Ben Zaken, Yoav Goldberg, and Shauli Ravfogel. Bitfit: Simple parameter-efficient fine-tuning for transformer-based masked language-models. In *Proceedings of the 60th Annual Meeting of the Association for Computational Linguistics (Volume 2: Short Papers)*, pages 1–9, 2022. 2
- [75] Maxime Zanella and Ismail Ben Ayed. Low-rank few-shot adaptation of vision-language models. In Proceedings of the IEEE/CVF Conference on Computer Vision and Pattern Recognition, pages 1593–1603, 2024. 7, 16
- [76] Qingru Zhang, Minshuo Chen, Alexander Bukharin, Nikos Karampatziakis, Pengcheng He, Yu Cheng, Weizhu Chen, and Tuo Zhao. Adalora: Adaptive budget allocation for parameter-efficient fine-tuning. arXiv preprint arXiv:2303.10512, 2023. 7
- [77] Renrui Zhang, Rongyao Fang, Wei Zhang, Peng Gao, Kunchang Li, Jifeng Dai, Yu Qiao, and Hong-sheng Li. Tip-adapter: Training-free clip-adapter for better vision-language modeling. arXiv preprint arXiv:2111.03930, 2021. 3, 7, 19
- [78] Renrui Zhang, Jiaming Han, Chris Liu, Peng Gao, Aojun Zhou, Xiangfei Hu, Shilin Yan, Pan Lu, Hongsheng Li, and Yu Qiao. Llama-adapter: Efficient fine-tuning of language models with zero-init attention. *arXiv preprint arXiv:2303.16199*, 2023. 3
- [79] Sheng Zhang, Yanbo Xu, Naoto Usuyama, Hanwen Xu, Jaspreet Bagga, Robert Tinn, Sam Preston, Rajesh Rao, Mu Wei, Naveen Valluri, Cliff Wong, Andrea Tupini, Yu Wang, Matt Mazzola, Swadheen Shukla, Lars Liden, Jianfeng Gao, Matthew P. Lungren, Tristan Naumann, Sheng Wang, and Hoifung Poon. Biomedclip: a multimodal biomedical foundation model pretrained from fifteen million scientific image-text pairs, 2024.
 3, 7
- [80] Zihao Zhao, Yuxiao Liu, Han Wu, Mei Wang, Yonghao Li, Sheng Wang, Lin Teng, Disheng Liu, Zhiming Cui, Qian Wang, et al. Clip in medical imaging: A comprehensive survey. arXiv preprint arXiv:2312.07353, 2023.
- [81] Kaiyang Zhou, Jingkang Yang, Chen Change Loy, and Ziwei Liu. Conditional prompt learning for vision-language models. In CVPR, pages 16816–16825, 2022. 1, 3, 6, 7, 19, 32, 33
- [82] Kaiyang Zhou, Jingkang Yang, Chen Change Loy, and Ziwei Liu. Learning to prompt for vision-language models. IJCV, 130(9):2337–2348, 2022. 1, 2, 3, 6, 7, 16, 19, 32, 33
- [83] Beier Zhu, Yulei Niu, Yucheng Han, Yue Wu, and Hanwang Zhang. Prompt-aligned gradient for prompt tuning. In Proceedings of the IEEE/CVF International Conference on Computer Vision, pages 15659– 15669, 2023. 7
- [84] Beier Zhu, Yulei Niu, Yucheng Han, Yue Wu, and Hanwang Zhang. Prompt-aligned gradient for prompt tuning, 2024. 7, 19, 32, 33
- [85] Didi Zhu, Zhongyi Sun, Zexi Li, Tao Shen, Ke Yan, Shouhong Ding, Kun Kuang, and Chao Wu. Model tailor: Mitigating catastrophic forgetting in multi-modal large language models. arXiv preprint arXiv:2402.12048, 2024. 3

Singular Value Few-shot Adaptation of Vision-Language Models

Supplementary Material

A Dataset Details

Following CoOp [82] and BiomedCoOp [39], we conducted extensive experiments on 11 natural and 10 biomedical classification benchmark datasets to evaluate the effectiveness of the proposed CLIP-SVD. The natural datasets include ImageNet [15], Caltech101 [17], OxfordPets [52], StanfordCars [40], Flowers102 [51], Food101 [8], FGVCAircraft [48], SUN397 [69], DTD [13], EuroSAT [22], and UCF101 [61]. The biomedical datasets consist of CTKidney [29], DermaMNIST [65, 14], Kvasir [55], RETINA [56, 41], LC25000 [7], CHMNIST [33], BTMRI [50], OCTMNIST [34], BUSI [3], COVID-QU-Ex [64], and KneeXray [10]. For distribution shift experiments, we also included ImageNetV2 [60], ImageNet-Sketch [67], ImageNet-A [24], and ImageNet-R [23]. Dataset statistics are provided in Tables S3 and S4.

B Detailed Hyperparameters

The hyperparameters reported in Tables S1 and S2 across both natural and biomedical datasets were carefully tuned based on benchmark type and dataset characteristics. A consistent batch size (BS) of 32 was maintained throughout to ensure uniformity in training dynamics. For natural datasets, the learning rate (LR) was set to 5×10^{-4} for few-shot settings and reduced to 6×10^{-4} for base-to-novel evaluations. For the natural few-shot setting, we follow [75] and set the number of iterations to $200 \times K$ (number of shots), whereas we use epochs for the base-to-novel setting, with the number of training epochs (EP) varying between 2 and 20 depending on the dataset's size. In biomedical datasets, LR values were more diverse, ranging from 0.5×10^{-3} to 20×10^{-3} , reflecting the varying difficulty and modality of the medical tasks, while EP was generally higher (up to 200) to accommodate the typically smaller dataset sizes and slower convergence. Notably, BUSI [3] lacked base-to-novel evaluation due to the absence of appropriate class splits.

C Domain Generalization

We evaluate the robustness of our method on out-of-distribution datasets. Similar to cross-dataset evaluation, we test our ImageNet-trained model directly on four other ImageNet datasets with different types of distribution shifts, including ImageNetV2 [60], ImageNet-Sketch (ImageNet-S) [67], ImageNet-A [24], and ImageNet-R [23]. Table S5 presents the domain generalization results, where methods are trained on ImageNet and evaluated on datasets with various domain shifts (-V2, -S, -A, and -R). CLIP-SVD achieves the highest average accuracy of 62.55%, outperforming MaPLe (62.36%) and other methods. It also leads in two target domains, namely ImageNet-S (-S) (+0.47%) and ImageNet-V2 (-V2) (+0.28%), demonstrating its robustness to domain shifts. These results highlight the effectiveness of CLIP-SVD in generalizing across domains.

D Effect of Rank-based Singular Value Selection for CLIP-SVD

For CLIP-SVD, selective finetuning of the singular values could further reduce the computational requirement. With singular value decomposition, the singular values are naturally ranked in a descending order, with respect to their magnitude. In this experiment, we varied the number of non-zero singular values out of the full rank to be adapted according to their ordering of magnitude, in order to investigate their impact on 4-shot model performance across both natural and biomedical domains. Specifically, we tested two configurations: one where only the top singular values (in the descending order) are finetuned and the other where only the bottom singular values (in the ascending order) are adjusted. The results shown in Fig. S1 reveal that, in the natural domain, both top and bottom configurations exhibit a steep initial accuracy increase starting from a small proportion of adjustable singular values, stabilizing near 78.18% as the ratio approaches full-rank, suggesting a limited sensitivity to the ranking of the selected singular values to be adapted. In contrast, the biomedical domain shows a more pronounced dependency on ranking of the adjustable singular

Dataset	Benchmark	BS	LR (10 ⁻⁴)	EP/IT
ImageNet	Few-shot		5	200
imagenet	Base-to-Novel	32	6	10
	Cross-dataset Transfer	32	5	2
	Domain Generalization	32	5	2
Caltech101	Few-shot	32	5	200
Cancellioi	Base-to-Novel	32	6	20
DTD	Few-shot	32	5	200
	Base-to-Novel	32	6	20
EuroSAT	Few-shot	32	5	200
	Base-to-Novel	32	6	20
StanfordCars	Few-shot	32	5	200
	Base-to-Novel	32	6	10
Flowers 102	Few-shot		5	200
Flowers 102	Base-to-Novel	32	6	10
FGVCAircraft	Few-shot	32	5	200
FGVCAlician	Base-to-Novel	32	6	20
SUN397	Few-shot	32	5	200
3011371	Base-to-Novel	32	6	10
OxfordPets	Few-shot	32	5	200
Oxidiareis	Base-to-Novel	32	6	10
UCF101	Few-shot	32	5	200
UCFIUI	Base-to-Novel	32	6	10
Food101	Few-shot	32	5	200
F000101	Base-to-Novel	32	6	10

-				
Dataset	Benchmark	BS	$LR (10^{-3})$	EP
BTMRI	Few-shot	32	7	100
BIMKI	Base-to-Novel	32	9	100
BUSI	Few-shot	32	2	100
	Base-to-Novel	-	-	-
COVID-OU-Ex	Few-shot	32	0.5	100
COVID-QU-EX	Base-to-Novel	32	2	50
CTKIDNEY	Few-shot	32	1	200
CIKIDNEY	Base-to-Novel	32	10	200
Kvasir	Few-shot	32	5	100
Kvasir	Base-to-Novel	32	3	60
CHMNIST	Few-shot	32	1	60
CHMINIST	Base-to-Novel	32	7	100
LC25000	Few-shot	32	3	100
LC23000	Base-to-Novel	32	10	100
RETINA	Few-shot	32	7	100
KETINA	Base-to-Novel	32	20	60
VmaaVmay	Few-shot	32	8	100
KneeXray	Base-to-Novel	32	2	60
OCTMNIST	Few-shot	32	10	100
OCTIVINIST	Base-to-Novel	32	20	100

Table S1: Hyperparameter values across natural Table S2: Hyperparameter values across biomedical datasets and benchmarks. (BS = Batch Size, LR = Learn-datasets and benchmarks. ing Rate, EP = Epochs, IT = Iterations)

(BS = Batch Size, LR = Learning Rate, EP = Epochs)

Table S3: Summary of natural datasets: Overview of the datasets used in the natural domain, including the number of classes, dataset splits (train, validation, test), and the corresponding handcrafted text prompts used for classification.

Dataset	Classes	Train	Val	Test	Hand-crafted prompt
ImageNet	1,000	1.28M	N/A	50,000	"a photo of a [CLASS]."
Caltech101	100	4,128	1,649	2,465	"a photo of a [CLASS]."
OxfordPets	37	2,944	736	3,669	"a photo of a [CLASS], a type of pet."
StanfordCars	196	6,509	1,635	8,041	"a photo of a [CLASS]."
Flowers	102	4,093	1,633	2,463	"a photo of a [CLASS], a type of flower."
Food101	101	50,500	20,200	30,300	"a photo of [CLASS], a type of food."
FGVCAircraft	100	3,334	3,333	3,333	"a photo of a [CLASS], a type of aircraft."
SUN397	397	15,880	3,970	19,850	"a photo of a [CLASS]."
DTD	47	2,820	1,128	1,692	"[CLASS] texture."
EuroSAT	10	13,500	5,400	8,100	"a centered satellite photo of [CLASS]."
UCF101	101	7,639	1,898	3,783	"a photo of a person doing [CLASS]."
ImageNetV2	1,000	N/A	N/A	10,000	"a photo of a [CLASS]."
ImageNet-Sketch	1,000	N/A	N/A	50,889	"a photo of a [CLASS]."
ImageNet-A	1,000	N/A	N/A	50,889	"a photo of a [CLASS]."
ImageNet-R	1,000	N/A	N/A	50,889	"a photo of a [CLASS]."

values. Here, finetuning the top singular values consistently outperforms the bottom configuration, reaching 68.02% at a full rank ratio, while the bottom approach lags behind by approximately 5% at the 0.5 ratio, highlighting the importance of prioritizing top singular values for specialized medical contexts.

Table S4: **Summary of biomedical datasets:** Overview of the datasets used in the biomedical domain, including the number of classes, dataset splits (train, validation, test), and the corresponding hand-crafted text prompts used for classification.

Dataset	Classes	Train	Val	Test	Hand-crafted prompt
CTKIDNEY	4	6,221	2,487	3,738	"a photo of a [CLASS]."
Kvasir	8	2,000	800	1,200	"a photo of a [CLASS]."
RETINA	4	2,108	841	1,268	"a photo of a [CLASS]."
LC25000	5	12,500	5,000	7,500	"a photo of a [CLASS]."
CHMNIST	8	2,496	1,000	1,504	"a photo of [CLASS]."
BTMRI	4	2,854	1,141	1,717	"a photo of a [CLASS]."
OCTMNIST	4	97,477	10,832	1,000	"a photo of a [CLASS]."
BUSI	3	389	155	236	"a photo of a [CLASS]."
COVID-Qu-Ex	4	10,582	4,232	6,351	"a chest xray of [CLASS]."
KneeXray	5	5,778	826	1,656	"a photo of a [CLASS]."

Table S5: **Domain generalization:** Methods are trained on ImageNet using 16-shots and evaluated on datasets with domain shifts (ImageNet-V2, -S, -A, and -R) for classification accuracy (%).

	Source		Target				
	ImageNet	-V2	-S	-A	-R	Avg.	
CLIP	66.73	60.83	46.15	47.77	73.96	59.09	
CoOp	71.51	64.20	47.99	49.71	75.21	61.72	
Co-CoOp	71.02	64.07	48.75	50.63	76.18	62.13	
CLIP-Adapter	68.46	59.55	39.88	38.83	64.62	54.27	
TIP-Adapter	53.81	45.69	29.21	36.04	55.26	44.00	
TIP-Adapter-F	51.71	43.07	27.13	27.04	45.07	38.80	
TaskRes	70.84	62.15	43.76	43.91	71.59	58.45	
KgCoOp	71.20	64.10	48.97	50.69	76.70	62.33	
ProGrad	72.24	64.73	47.61	49.39	74.58	61.71	
MaPLe	70.72	64.07	49.15	50.90	76.98	62.36	
CLIP-SVD	72.15	65.03	49.62	49.17	76.79	62.55	

E Experiments with Other Backbones

In this experiment, we evaluated our proposed method, CLIP-SVD, using the alternative ViT-B/32 backbone in a few-shot learning setting for the natural domain. Table S6 presents the average classification accuracy (%) across 11 natural domain benchmarks derived from three randomly sampled support sets for each dataset. Our method consistently outperforms the state-of-the-art techniques across different few-shot settings. Notably, CLIP-SVD achieves the highest performance in all cases, surpassing the second-best method, Tip-Adapter-F, by a significant margin, with an improvement of approximately 1.2% at K=1 and 1.4% at K=16. These results highlight the strength of our singular value decomposition-based adaptation strategy in enhancing generalization under limited data conditions. Furthermore, the effectiveness of CLIP-SVD with the ViT-B/32 backbone demonstrates that our approach is adaptable to different model backbones, making it broadly applicable across various vision-language models.

F TextSpan Analysis Details

We analyze singular value shifts in the Output-Value (OV) circuit using TextSpan [18], focusing on the last four layers (L8–L11) of CLIP and BiomedCLIP ViT-B/16 (*Note: layer and head indexing in these experiments begins at 0.*). The ViT-B/16 vision encoder employs 12 attention heads per MHSA block. For the natural image domain, we use ImageNet [15], while for the biomedical domain, we aggregate all relevant datasets [29, 55, 56, 41, 7, 33, 50, 34, 3, 64, 10] into a single comprehensive dataset. Images from both domains are fed into their corresponding vision

Table S6: Evaluation against state-of-the-art techniques for natural domain with ViT-B/32 backbone: This table presents the average classification accuracy (%) obtained from 11 natural domain benchmarks derived from 3 sampled support sets for each dataset. The top-performing results are in bold, and the second-best are underlined.

Method	K = 1	K = 2	K = 4	K = 8	K = 16
Zero-shot CLIP [57]			61.8		
CoOp [82]	62.8	65.3	68.6	72.2	74.7
CoCoOp [81]	63.1	64.8	66.7	68.1	70.7
ProGrad [84]	64.7	67.1	69.8	73.2	75.9
KgCoOp [71]	64.9	66.6	68.4	70.5	72.1
MaPLe [35]	61.5	65.2	68.7	71.6	74.1
CLIP-Adapter [19]	62.5	63.5	64.3	67.6	71.6
Tip-Adapter-F [77]	66.5	69.2	<u>71.6</u>	<u>74.1</u>	<u>77.1</u>
CLIP-SVD (Ours)	67.7	71.0	73.4	75.8	78.5

Table S7: **Natural Domain Efficiency comparison** of different parameter-efficient tuning methods. We report trainable parameter counts, training, and inference time.

Method	Trainable Params	Training Time (min)	Inference Time (s)
CoOp	2.0K	1.84	7.34
CoCoOp	35.4K	2.25	18.52
MaPLe	3.5M	2.95	7.40
CLIP-Adapter	131.1K	4.93	7.48
Tip-Adapter	0	_	24.97
TCP	331.9K	1.02	7.58
CLIP-LoRA	184.3K	9.82	7.41
CLIP-SVD (Ours)	92.2K	0.88	7.13

Table S8: **Biomedical Domain Efficiency comparison** of different parameter-efficient tuning methods. We report trainable parameter counts, training, and inference time.

Method	Trainable Params	Training Time (min)	Inference Time (s)
CoOp	2.0K	1.19	7.20
CoCoOp	44.8K	0.58	23.6
MaPLe	5.3M	2.4	19.8
CLIP-Adapter	131.1K	2.85	7.79
Tip-Adapter	0	-	23.52
DCPL	5.5M	2.58	177.6
BiomedCoOp	3.1K	1.76	7.20
CLIP-LoRA	221.2K	10.25	7.58
CLIP-SVD (Ours)	110.6K	1.78	6.76

encoder network. For the natural domain, we utilize the text corpus from [18], which consists of approximately 3,000 GPT-3.5-generated general image descriptions. In contrast, no large-scale text corpus exists for biomedical images. To address this, we generated a new corpus comprising 300 general medical image descriptions and relevant terminologies using GPT-4 [1]. We use the following prompt to query GPT-4: "Generate 300 distinct descriptive prompts for medical images that capture specific visual features commonly found in medical scans, such as contrast, shape, color, location, and texture." Using TextSpan, we extract the top three text descriptions from the corpus that best characterize the role of each attention head in each of the final four layers. Based on these top-3 descriptions, GPT-4 is used to assign a concise and descriptive title to each head's function: "Assign a concise and descriptive title that best captures the primary function represented by these descriptions.". The identified roles and associated top-3 descriptions for each head in layers L8–L11 for the natural and biomedical domains are detailed in Tables S10 and S11 respectively.

G t-SNE Visualization

We used t-SNE [66] to visualize the image embeddings generated by the fine-tuned model using our CLIP-SVD and compared them with the embeddings from the pre-trained CLIP and BiomedCLIP models. As shown in Figure S3, the embeddings produced by CLIP-SVD exhibit significantly better clustering, indicating that our method enables the model to generate more distinct and well-separated feature representations. This experiment was conducted on the EuroSAT, OxfordPets, CTKidney, and

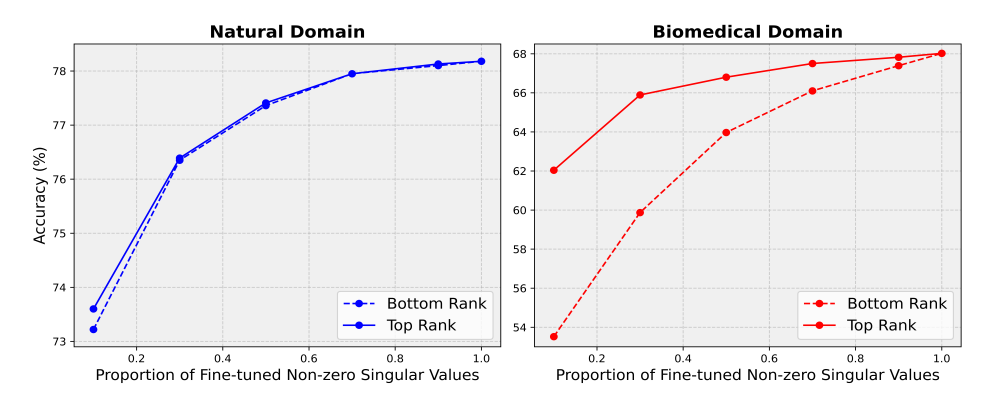


Figure S1: Accuracy comparison for models finetuned with varying rank ratios in the natural (left) and biomedical (right) domains

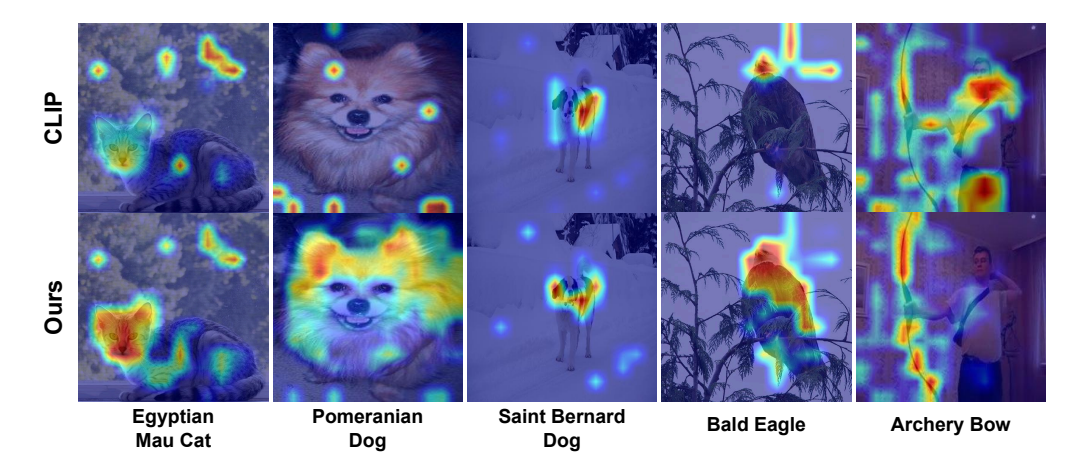


Figure S2: Saliency map comparison between the pre-trained CLIP model and the CLIP-SVD fine-tuned model. The adapted model shows more focused and semantically aligned attention, highlighting improved localization of relevant image regions.

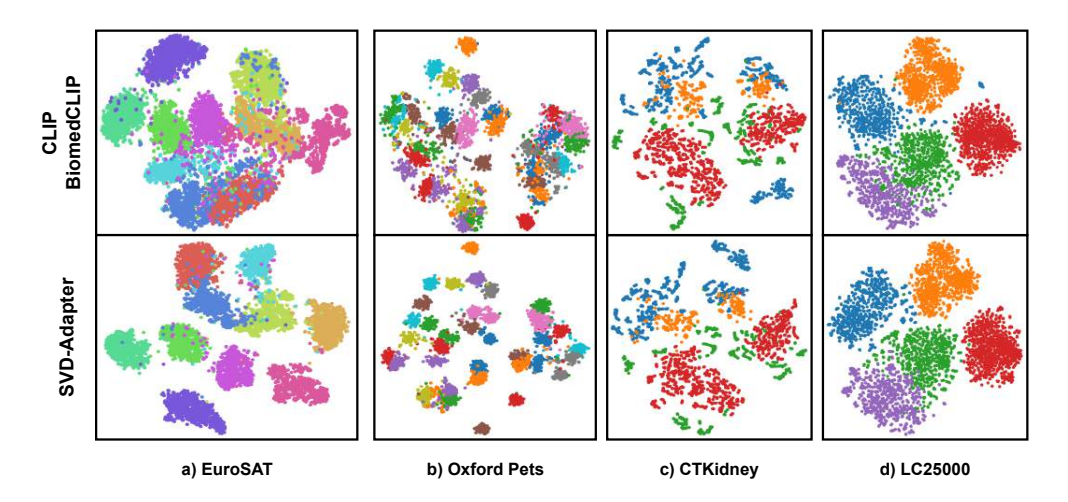


Figure S3: **t-SNE visualization of image embeddings:** Comparison of embeddings produced by the pre-trained CLIP/BiomedCLIP model and the fine-tuned CLIP-SVD on (a) EuroSAT, (b) Oxford Pets, (c) CTKidney, and (d) LC25000. CLIP-SVD generates more compact and well-separated clusters, indicating improved feature extraction and task-specific alignment.

LC25000 datasets, where the improved clustering patterns highlight the enhanced feature extraction capabilities of our approach.

H Segmentation Performance

We evaluated the segmentation performance of our finetuned model using the TextSpan algorithm [18] on the ImageNet-Segmentation dataset [20], a curated subset of 4,276 ImageNet validation images with pixel-level annotations, and compared the results against those of the original pre-trained CLIP model. To perform segmentation, we follow the approach introduced in the TextSpan framework [18], which builds on a fine-grained decomposition of CLIP's image representation. Specifically, we use the fact that the CLIP image encoder's output can be expressed as a sum over attention head contributions across

Model	Pixel Acc.	mIoU	mAP
CLIP	77.24	57.73	82.62
CLIP-SVD (Ours)	77.55	58.27	82.82
Δ	+0.31	+0.54	+0.20

Table S9: Segmentation Performance in terms of pixel accuracy, mean IoU, and mean average precision (%).

spatial positions. Each image patch contributes a vector in the shared image-text embedding space. Given a text prompt corresponding to the object class (i.e. "an image of a [CLASS]"), we compute a heatmap by measuring the similarity between each patch's contribution and the CLIP embedding of the text description. These similarity scores are then aggregated into a spatial map that highlights the regions most semantically aligned with the prompt. We also used gScoreCAM [11] to visualize saliency maps for both the pre-trained CLIP model and the version fine-tuned with CLIP-SVD. Table S9 shows the results in terms of pixel accuracy, mean intersection over union (mIoU), and mean average precision (mAP). Our method achieves a performance boost across all metrics, with a gain of +0.31% in pixel accuracy, +0.54% in mIoU, and +0.20% in mAP. These improvements demonstrate that CLIP-SVD enhances the model's ability to localize and segment fine-grained regions in complex natural images, leading to more accurate and consistent segmentation results. This boost in segmentation performance stems from improved feature extraction and attention alignment through singular value adaptation as indicated in Section 4.6. Fine-tuning the singular values helps the model's attention heads capture task-relevant features, such as geographic cues in EuroSAT and color-related patterns in Oxford Pets, as shown in Figure S2. This enables better foreground-background differentiation and more precise segmentation boundaries, explaining the observed performance gains.

I Computational Cost

We present detailed results in Tables S7 and S8, comparing various PEFT methods in terms of total trainable parameters, training time, and inference time on the DTD and RETINA datasets, respectively. This analysis highlights the performance–efficiency trade-off across methods. All experiments were conducted on a single NVIDIA A100 GPU with 40GB of RAM, using a batch size of 8 at inference for consistency and fairness. The results demonstrate that CLIP-SVD strikes a favorable balance: it requires relatively few trainable parameters, converges more quickly, and introduces no inference overhead, while achieving high accuracy in few-shot settings. Moreover, CLIP-SVD avoids reliance on external modules or architectural modifications, simplifying deployment and improving efficiency, particularly in low-resource or latency-sensitive scenarios.

J Additional Per-dataset Results

We provide the complete per-dataset few-shot results for both the natural and biomedical domains to offer a detailed evaluation of our method's performance. The natural and biomedical domain results are summarized in Tables S12 and S13, respectively, which report the classification accuracy across different few-shot settings for each individual dataset. On the other hand, we offer the per-dataset base-to-novel generalization results in Table S14 and S15. This detailed breakdown highlights the consistent improvement achieved by CLIP-SVD over state-of-the-art methods, demonstrating its ability to generalize effectively across diverse datasets and domains.

Table S10: Natural Domain Analysis of the attention heads of each layer with the top 3 descriptions returned by TextSpan [18]. Here, "L" denotes layer while " \mathbf{H} " denotes attention head.

ciumed by Texispan [16]. Here, L denotes lay	el wille II denotes attention head.
L8.H0: Foundational Shapes & Silhouettes	L8.H1: Motion & Directional Cues
Rural windmill silhouette A plank Intricate clock mechanism	Dynamic sports action shot Tranquil boating on a lake Lively city parade
L8.H2: Contrast & Light-Dark Regions	L8.H3: Geometric Patterns & Grids
Photograph with the artistic style of fisheye lens Psychedelic color swirls Sunlit meadow path	Artwork featuring Morse code typography Cubist still life painting Miniature diorama photography
L8.H4: Object Boundaries & Contours	L8.H5: Repeated Structures & Textures
Cinematic portrait with dramatic lighting A whirlpool Image with harlequin patterns	Plaid pattern Reflective surfaces Image of a scooter
L8.H6: Refined Textural Details of Everyday Objects	L8.H7: Positional Layout & Spatial Balance
Collage of textures Close-up of a textured bark Mesmerizing kinetic sculpture	Cozy cabin interior Minimalist white backdrop Rolling vineyard landscapes
L8.H8: Edge Detection & Detail Refinement	L8.H9: Primitive Forms & Visual Anchors
A scalene quadrilateral Minimalist architectural photography Detailed charcoal sketch	Dappled sunlight A cloverleaf Ocean sunset silhouette
L8.H10: Coarse-to-Fine Visual Transitions	L8.H11: Structural Symmetry & Alignment
Intricate wood carving Contemplative monochrome portrait Aerial view of a marketplace	Birds-eye view Detailed illustration of a futuristic brain-computer interface Tranquil garden pathway
L9.H0: Scene Composition & Perspective	L9.H1: Depth Perception & Visual Planes
Aerial view of a marketplace Glowing neon cityscape Playful siblings	A zoomed out photo Classic black and white cityscape Antique historical artifact
L9.H2: Interaction Between Objects	L9.H3: Material Surfaces & Reflection
An image of a Gymnast Emotional and heartfelt human connection Detailed illustration of a futuristic brain-computer interface	Aerial view of a teeming rainforest Inviting reading nook e Dynamic and high-energy dance competition
L9.H4: Natural Landscapes & Textures	L9.H5: Architectural Layouts & Forms
Aerial view of a vineyard Enchanting forest nymph aesthetic Delicate and intricate lace patterns	Photograph showcasing laughter Minimalist architectural photography Urban labyrinth
L9.H6: Facial Features & Gaze Cues	L9.H7: Semantic Grouping of Elements
Detailed charcoal sketch Intense water sports moment Photograph with the artistic style of light trails	Urban rooftop panorama Cozy cabin interior Photo taken in the Japanese tea gardens
L9.H8: Soft Lighting & Shadow Play	L9.H9: Organic Flow & Movement
Impressionist portrait painting Intriguing and enigmatic passageway Ephemeral soap bubble pattern	Photograph with abstract geometric overlay Artwork featuring Morse code typography Abstract oil painting
L9.H10: Conceptual Boundaries & Themes	L9.H11: Temporal Sequences & Visual Narratives
Miniature diorama photography emotional candid moment	Colorful hot air balloons Picture taken in Rwanda

Table S10 (continued): Natural Domain Analysis of the attention heads of each layer with the top 3 descriptions returned by TextSpan [18]. Here, "L" denotes layer while "H" denotes attention head.

L10.H0: Aerial Landscapes & Environments	L10.H1: Human Experiences & Objects in Action
Aerial view of an agricultural field Image taken in the Namibian desert Picture taken in the Brazilian rainforest	Hands in an embrace Dynamic and high-energy music concert Emergency Medical Technician at work
L10.H2: Cultural & Textural Scenes	L10.H3: Colorful Festivities & Patterns
Picture taken in the Spanish Flamenco festivals Ornate wood carving Image captured in the Peruvian Andes	Lively and colorful parade Tie-dye design Soft pastel tones
L10.H4: Cozy Indoors & Historical Locations	L10.H5: Action, Emotion & Faces
Photograph taken in a retro diner Picture taken in the Scottish castles Cozy living room ambiance	Dynamic Action Energetic children Playful winking facial expression
L10.H6: Organic Forms & Flow	L10.H7: Geographic & Cultural Diversity
Graceful wings in motion Curved organic designs Ethereal double exposure photography	Picture taken in Pakistan Bustling cultural market Image snapped in the Swiss chocolate factories
L10.H8: Color & Design Aesthetics	L10.H9: Sketches, Illustrations & Concepts
Photograph with a yellow color palette Photo taken in the Brazilian samba parade Colorful hot air balloons	Collage of vintage magazine clippings Detailed charcoal sketch Impressionist-style digital painting
L10.H10: Mood, Atmosphere & Highlights	L10.H11: Human-Centered Realism & Objects
Image with holographic retro synthwave aesthetics Serene lakeside cabin Whirlpool of brimstone	Urban labyrinth Image of a police car Intricate gemstone arrangement
L11.H0: Semantic Layout & Spatial Context	L11.H1: Human Relationships & Portraiture
Mysterious day scene Urban rooftop panorama A zoomed out photo	Images of people and emotional interaction Family portraits and group dynamics Visuals of children, couples, and professionals
L11.H2: Numbers, Symbols & Temporal Cues	L11.H3: Lifestyle & Tranquil Activities
Digits and symbolic representations in images Temporal cues like clocks, sunsets, motion blur Confetti, reflections, and expressive timing	Calm urban and rural lifestyle scenes Tranquil locations: diners, libraries, markets Cozy homes, beach sunsets, fairgrounds
L11.H4: Visual Symbols & Cultural Motifs	L11.H5: Rare Words & Abstract Concepts
Cultural symbols and calligraphy art Caricatures, retro TV test patterns, mystical motifs Architectural and folkloric aesthetics	Abstract words (quasar, zephyr), letter imagery Rare geographic terms, numerals, and geometry Conceptual elements and visual abstractions
L11.H6: Global Geographic Locations	L11.H7: Color Themes & Tonal Palettes
Images tied to global cities and landmarks Natural and urban landscapes across continents Famous locations: Machu Picchu, Santorini, NYC	Dominant color schemes (red, blue, gray) Pastel, sepia tones, artistic overlays Color-coded compositions and political art
L11.H8: Weather & Natural Forces	L11.H9: Everyday Objects & Refined Details
Storms, fog, lightning, and natural disasters Atmospheric effects and visual phenomena Wildlife amidst dynamic weather elements	Common items like scarves, bowls, wallets Mechanisms, furniture, modern artifacts Textures: wood grain, bubble, fabric
L11.H10: Natural Flora, Landscapes & Tranquility	L11.H11: Living Creatures & Natural Forms
Floral and plant life in serene settings Natural scenes: cherry blossoms, forests Geographic tranquility and biodiversity	Wide range of animals: dogs, elephants, fish Insects, feathers, natural surface textures Shells, fur, fruit, snowflakes

Table S11: Biomedical Domain Analysis of the attention heads of each layer with the top 3 descriptions returned by TextSpan [18]. Here, "L" denotes layer while "H" denotes attention head.

ons returned by Textspan [16]. Here, L de	-
L8.H0: Focal Markers & Shape Cues	L8.H1: Peripheral Edges & Enhancement Rings
Target signs and air bronchograms Geographic zones of tissue involvement	Ring-enhancing lesions and peripheral edema Pseudocapsules and symmetric deviations
Microcalcifications and pseudocapsule patterns	Finger-in-glove signs and disruption of growth plates
L8.H2: Lobe Collapse & Serpentine Patterns	L8.H3: Radiologic Artifacts & Diffuse Shapes
Collapsed lobes and reverse halo signs	Comet-tail artifacts and nodular regions
Serpiginous lesions and high signal regions	Fluid levels suggesting benignity
Growth plate disruptions and cortical thinning	Asymmetries and contrast-enhanced zones
L8.H4: Flow Voids & Vascular Boundaries	L8.H5: Textural Shifts & Patchy Regions
An area with decreased perfusion	Mosaic attenuation and necrotic centers
A vascular displacement	Patchy regions with blurry margins
A vascular structure with sharp borders	Air bronchograms and target-like patterns
L8.H6: Contour Irregularity & Internal Spread	L8.H7: Symmetry Deviation & Dense Regions
An anatomical displacement	Mass effect and asymmetry in dense zones
A spiculated margin	Patchy consolidations and star-shaped opacities
A zone of tissue infiltration	Air bronchograms and peri-lesional edema
L8.H8: Clustered Signals & Midline Shifts	L8.H9: Scattered Highlights & Artifactual Spots
Midline shifts with hyperintense clustering	An area with decreased perfusion in the left hemisphere
Target signs and septated fluid collections	A bright spot artifact in a clustered pattern
Cortical thinning and pseudocapsule formations	A contrast-enhanced region on axial view
L8.H10: Diffuse Zones & Overlapping Shapes	L8.H11: Dense Regions & Local Signal Buildup
Donut and target signs in scattered areas	Zones of infiltration with surrounding edema
Diffuse abnormalities and cross-compartment lesions	Septated collections and mass effects
Hypo- and hyperintense signals across lobes	Contrast enhancement and vascular structures
L9.H0: Symmetry Shifts & Linear Features	L9.H1: Ring-Like Structures & Localized Spread
A deviation from expected symmetry in the left hemisphere	A central necrosis in a scattered distribution
A serpiginous lesion in the left hemisphere	A crescent-shaped fluid collection in a scattered distribution
A well-defined border suggesting benignity	A deviation from anatomical landmarks consistent with inflammation
L9.H2: Irregular Densities & Textured Borders	L9.H3: Small Patterned Anomalies
A beam-hardening artifact	A tree-in-bud pattern without enhancement
A collapsed lung lobe without enhancement	A cavitary lesion without enhancement
A peripherally enhancing collection with sharp borders	A high signal-to-noise ratio with sharp borders
L9.H4: Defined Edges & Subpleural Zones	L9.H5: Streaks, Texture, & Soft Borders
A subpleural nodule	A zone of tissue infiltration with surrounding edema
A central necrosis in a scattered distribution	A tram-track sign in the left hemisphere
A lesion crossing compartments	A striated muscle texture
L9.H6: Sharp Edges & Tissue Mismatch	L9.H7: Thickened Zones & Star-Like Forms
An anatomical displacement	A region of tissue thickening
An irregular border with surrounding edema	A star-shaped opacity in the upper lobe
A streak artifact	A contrast-enhanced region
L9.H8: Homogeneous Textures & Clustered Lines	L9.H9: Contour Disruptions & Shape Markers
A lesion with fluid level	A cystic lesion suggesting benignity
A homogeneous texture	A reverse halo sign
A disruption of normal anatomy	A triangular-shaped defect
L9.H10: Circumscribed Lesions & Flow Paths	L9.H11: Signal Artifacts & Internal Septations
A well-circumscribed lesion	A comet-tail artifact
A cluster of microcalcifications suggesting malignancy	A lesion with internal septations without enhancement
A serpiginous lesion in the left hemisphere	A motion artifact

Table S11 (continued): Biomedical Domain Analysis of the attention heads of each layer with the top 3 descriptions returned by TextSpan [18]. Here, "L" denotes layer while "H" denotes attention head.

descriptions returned by TextSpan [18]. Here, "L"	denotes layer while "H" denotes attention hea
L10.H0: Low-Contrast Regions & Collapse Patterns	L10.H1: Localized Irregularities & Shadowing
A collapsed lung lobe A vascular structure with sharp borders A focal area of calcification in the left hemisphere	A deviation from anatomical landmarks A lytic lesion consistent with inflammation A finger-in-glove sign in the left hemisphere
L10.H2: Contrast Rings & Interface Blur	L10.H3: Multi-Compartment Spread & Fine Edges
An air bronchogram suggesting malignancy A blurring of tissue interfaces A peripherally enhancing collection consistent with infection	A lesion crossing compartments in the left hemisphere A miliary pattern A vascular structure with sharp borders
L10.H4: Fused Regions & Curved Forms	L10.H5: Sharp Transitions & Highlighted Foci
A finger-in-glove sign in the left hemisphere A region with cortical thinning with surrounding edema A lesion with fluid level suggesting benignity	A streak artifact A targetoid lesion A cluster of microcalcifications suggesting malignancy
L10.H6: Circular Opacities & Clean Boundaries	L10.H7: Textured Rings & Septated Centers
A circular opacity A septated fluid collection A clean fluid interface	A central necrosis A lesion with calcified rim A reverse halo sign
L10.H8: Artifact-Like Patterns & Symmetry Shift	L10.H9: Smooth Outlines & Diffuse Flow
A midline shift in a clustered pattern A beam-hardening artifact A disruption of growth plate suggesting benignity	A serpiginous lesion in the left hemisphere A stenotic segment in the upper lobe A lesion with irregular internal architecture
L10.H10: Star Patterns & Linear Disruptions	L10.H11: Texture Aggregates & Uniform Zones
A star-shaped opacity in the upper lobe A shifting fluid level A motion artifact suggesting benignity	A lytic lesion on axial view A honeycomb pattern A sunburst pattern suggesting benignity
L11.H0: Signal Voids & Midline Shifts	L11.H1: Blurred Regions & Artifact Shapes
A collapsed lung lobe A low signal-to-noise ratio in the upper lobe A lesion crossing compartments	A solid-cystic component suggesting malignancy A finger-in-glove sign in a scattered distribution A double-density sign suggesting benignity
L11.H2: Peripheral Contrast & Mosaic Attenuation	L11.H3: Cross-Lobe Flow & Density Buildup
A mosaic attenuation A geographic area of involvement in the upper lobe A peripherally enhancing collection consistent with infection	A cavitary lesion without enhancement A lesion crossing compartments A shifting fluid level
L11.H4: Sharp Fluid Interfaces & Contrast Pockets	L11.H5: Ringed Zones & Pattern Complexity
A tram-track sign on axial view A clean fluid interface A central necrosis with sharp borders	A targetoid lesion A fluid-fluid level suggesting malignancy A mosaic attenuation
L11.H6: Rounded Opacities & Midline Distortions	L11.H7: Compact Signal Shifts & Grid-Like Forms
A circular opacity A solid-cystic component suggesting malignancy A crescent-shaped fluid collection	A star-shaped opacity in the upper lobe A widened mediastinum A spiculated margin
L11.H8: Converging Edges & Cluster Markers	L11.H9: Scattered Intensity & Symmetry Cues
A low-contrast region in a clustered pattern A double-density sign suggesting benignity A solid-cystic component suggesting malignancy	A midline shift A disruption of normal anatomy A clean fluid interface
L11.H10: Rimmed Signals & Flow Distributions	L11.H11: Sharp Vascular Lines & Compact Zones
A peripherally enhancing collection consistent with infection A change in signal intensity suggesting malignancy A beam-hardening artifact	A vascular structure with sharp borders A cluster of microcalcifications suggesting malignanc A homogeneous texture
A change in signal intensity suggesting malignancy	A cluster of microcalcifications suggesting maligna

Table S12: **Natural per-dataset performance** comparison of with various methods in few-shot setting in terms of classification accuracy (%).

Dataset	Method	K=1	K = 2	K = 4	K = 8	K = 16
	CLIP			66.72		
	CLIP-Adapter	67.93	68.60	69.56	70.20	71.60
	Tip-Adapter	68.80	68.90	69.68	70.01	70.36
	Tip-Adapter-F	67.43	68.60	69.86	71.40	73.10
	Linear Probing	31.30	43.83	54.20	61.93	67.27
I NI.4	LP++	69.29	69.63	70.80	72.10	72.95
ImageNet	CoOp	65.77	68.17	69.38	70.83	71.51
	CoCoOp	69.51	69.84	70.55	70.77	71.02
	KgCoOp	69.03	69.63	70.19	70.23	71.2
	ProGrad	64.33	66.12	70.21	71.10	72.68
	MaPLe	62.67	65.10	67.70	70.30	72.33
	CLIP-SVD (Ours)	70.03	70.68	71.46	72.36	73.25
	CLIP			93.31		
	CLIP-Adapter	93.30	93.67	94.00	94.27	94.57
	Tip-Adapter	93.08	93.43	94.19	94.21	94.50
	Tip-Adapter-F	93.56	94.22	95.06	95.20	95.79
	Linear Probing	80.08	87.00	92.27	93.85	95.35
	LP++	92.85	94.14	94.87	95.44	95.94
Caltech101	СоОр	92.37	92.83	94.44	94.10	95.50
	CoCoOp	93.80	94.92	94.98	95.11	95.19
	KgCoOp	94.13	94.20	94.65	94.97	95.03
	ProGrad	90.96	93.21	94.93	94.92	95.80
	MaPLe	92.57	93.21	94.43	95.20	96.00
	CLIP-SVD (Ours)	93.91	94.44	95.12	95.85	96.17
	CLIP	1	0	44.09	00100	
	CLIP-Adapter	45.20	47.87	53.83	66.40	71.17
	Tip-Adapter	50.24	52.44	57.64	61.92	65.68
	Tip-Adapter-F	53.25	56.32	62.09	67.28	72.05
	Linear Probing	36.03	46.02	56.01	63.71	69.82
	LP++	52.34	$\frac{40.02}{56.05}$	62.17	67.30	
DTD						71.41
	CoOp	49.00	51.70	58.57	64.70	68.63
	CoCoOp	48.51	52.02	54.79	58.92	63.78
	KgCoOp	52.50	55.73	58.31	65.87	69.37
	ProGrad	52.79	54.35	57.72	62.13	65.92
	MaPLe	52.13	55.50	61.00	66.50	71.33 72.42
	CLIP-SVD (Ours)	56.05	60.60	64.83	68.28	12.42
	CLIP			48.37		
	CLIP-Adapter	61.70	66.07	66.80	73.23	81.87
	Tip-Adapter	62.46	64.65	70.39	71.57	78.44
	Tip-Adapter-F	63.95	70.38	76.43	81.11	87.46
	Linear Probing	56.36	59.56	71.90	77.93	85.45
EuroSAT	LP++	65.02	67.99	74.00	76.32	84.63
	CoOp	54.80	61.20	68.62	75.53	83.60
	CoCoOp	55.71	46.24	63.83	68.26	73.82
	KgCoOp	60.83	68.97	71.06	72.37	74.93
	ProGrad	55.10	66.19	70.84	79.22	84.38
	MaPLe	71.80	78.30	84.50	87.73	92.33
	CLIP-SVD (Ours)	75.06	83.30	84.65	89.74	92.68

Table S12 (continued): Natural per-dataset performance comparison of with various methods in few-shot setting in terms of classification accuracy (%).

StanfordCars StanfordCars StanfordCars StanfordCars Co Co Kg Prr Ma CI CI CI Ti Ti Ti Lin Co Co Kg Prr Co Co Co Kg Prr Co Co Kg Prr Ma CI Lin Ti Ti Lin Lin Lin Lin Co Co Kg Pre Ma CI	LIP LIP-Adapter p-Adapter p-Adapter-F near Probing P-H OOP COOP gCoOp oGrad aPLe LIP-SVD (Ours) LIP LIP-Adapter p-Adapter-F near Probing P-H OOP DOOP DOOP DOOP DOOP DOOP DOOP DOOP	67.10 66.47 67.88 33.70 66.31 67.10 67.92 67.03 67.11 66.60 70.56 54.83 80.74 86.63 72.50 86.22 71.98 82.20 74.63 83.81 83.30 83.25	68.97 68.03 71.39 48.93 70.41 69.37 68.77 68.13 71.94 71.60 73.15 54.83 86.59 90.21 85.48 90.38 76.12 88.47 79.47 88.62 88.93	65.63 71.13 70.08 74.59 62.34 74.57 72.73 69.10 71.98 71.75 75.30 77.25 70.81 54.83 89.62 91.50 91.65 92.96 82.56 91.14 90.69 89.98 92.67	76.47 71.61 78.34 71.21 76.12 76.57 70.19 73.53 78.78 79.47 81.10 56.08 92.15 94.98 95.25 84.17 94.37 89.53 93.51 95.80	80.90 74.08 83.09 80.10 80.77 78.89 71.68 74.87 81.46 83.57 84.98 56.50 93.68 96.18 97.36 96.44 87.64 96.10 92.90 94.87 97.00
StanfordCars Tip Tip Lin Lin Lin Lin Co Co Kg Pro Ma CI Ci Tip Tip Lin Lin Ci Ci Ci Ci Ci Ci Ci	p-Adapter p-Adapter p-Adapter-F mear Probing P++ pOp pCoOp gCoOp gGrad aPLe _IP-SVD (Ours) IP _IP-Adapter p-Adapter p-Adapter p-Adapter-F mear Probing P++ pOp pCoOp gCoOp gCoOp gCoOp gCoOp gCoOp gCoOp	66.47 67.88 33.70 66.31 67.10 67.92 67.03 67.11 66.60 70.56 54.83 80.74 86.63 72.50 86.22 71.98 82.20 74.63 83.81 83.30	68.03 71.39 48.93 70.41 69.37 68.77 68.13 71.94 71.60 73.15 54.83 86.59 90.21 85.48 90.38 76.12 88.47 79.47 88.62 88.93	70.08 74.59 62.34 74.57 72.73 69.10 71.98 71.75 75.30 77.25 70.81 54.83 89.62 91.50 91.65 92.96 82.56 91.14 90.69 89.98	71.61 78.34 71.21 76.12 76.57 70.19 73.53 78.78 79.47 81.10 56.08 92.15 94.98 95.89 95.25 84.17 94.37 89.53 93.51	74.08 83.09 80.10 80.77 78.89 71.68 74.87 81.46 83.57 84.98 56.50 93.68 96.18 97.36 96.44 87.64 96.10 92.90 94.87
StanfordCars StanfordCars StanfordCars Flowers 102 Flowers 102 Flowers 102 CL CL Tip Tip Lin Cc Cc Kg Pro Cc Cc Cc Kg Pro Cc Cc Cc Cc Cc Cc Cc Kg Pro Cc	p-Adapter-F mear Probing P++ pOp pCoOp gCoOp gCoOp oGrad aPLe LIP-SVD (Ours) LIP LIP-Adapter p-Adapter p-Adapter-F mear Probing P++ pOp pCoOp gCoOp gCoOp gCoOp gCoOp gCoOp	67.88 33.70 66.31 67.10 67.92 67.03 67.11 66.60 70.56 54.83 80.74 86.63 72.50 86.22 71.98 82.20 74.63 83.81 83.30	71.39 48.93 70.41 69.37 68.77 68.13 71.94 71.60 73.15 54.83 86.59 90.21 85.48 90.38 76.12 88.47 79.47 88.62 88.93	74.59 62.34 74.57 72.73 69.10 71.98 71.75 75.30 77.25 70.81 54.83 89.62 91.50 91.65 92.96 82.56 91.14 90.69 89.98	78.34 71.21 76.12 76.57 70.19 73.53 78.78 79.47 81.10 56.08 92.15 94.98 95.89 95.25 84.17 94.37 89.53 93.51	83.09 80.10 80.77 78.89 71.68 74.87 81.46 83.57 84.98 56.50 93.68 96.18 97.36 96.44 87.64 96.10 92.90 94.87
StanfordCars Lin LP Co Co Kg Pro Ma CL CL Tip Tip Lin Lin Co Co Kg Pro Co Co Co Kg Pro Co Co Kg Pro Co Co Kg Pro Ma CL Cl Cl Tip Tip Lin Lin Lin Lin Lin Lin Co Co Kg Pro Ma CL Cl Cl Cl Cl Cl Cl Cl Tip Tip Lin	near Probing P++ DOP	33.70 66.31 67.10 67.92 67.03 67.11 66.60 70.56 54.83 80.74 86.63 72.50 86.22 71.98 82.20 74.63 83.81 83.30	48.93 70.41 69.37 68.77 68.13 71.94 71.60 73.15 54.83 86.59 90.21 85.48 90.38 76.12 88.47 79.47 88.62 88.93	62.34 74.57 72.73 69.10 71.98 71.75 75.30 77.25 70.81 54.83 89.62 91.50 91.65 92.96 82.56 91.14 90.69 89.98	71.21 76.12 76.57 70.19 73.53 78.78 79.47 81.10 56.08 92.15 94.98 95.89 95.25 84.17 94.37 89.53 93.51	80.10 80.77 78.89 71.68 74.87 81.46 83.57 84.98 56.50 93.68 96.18 97.36 96.44 87.64 96.10 92.90 94.87
StanfordCars	or ++ or op	66.31 67.10 67.92 67.03 67.11 66.60 70.56 54.83 80.74 86.63 72.50 86.22 71.98 82.20 74.63 83.81 83.30	70.41 69.37 68.77 68.13 71.94 71.60 73.15 54.83 86.59 90.21 85.48 90.38 76.12 88.47 79.47 88.62 88.93	74.57 72.73 69.10 71.98 71.75 75.30 77.25 70.81 54.83 89.62 91.50 91.65 92.96 82.56 91.14 90.69 89.98	76.12 76.57 70.19 73.53 78.78 79.47 81.10 56.08 92.15 94.98 95.89 95.25 84.17 94.37 89.53 93.51	80.77 78.89 71.68 74.87 81.46 83.57 84.98 56.50 93.68 96.18 97.36 96.44 87.64 96.10 92.90 94.87
StanfordCars	oOp oCoOp gCoOp gCoOp oGrad aPLe LIP-SVD (Ours) LIP LIP-Adapter p-Adapter p-Adapter-F near Probing P++ oOp oCoOp gCoOp gCoOp oGrad aPLe	67.10 67.92 67.03 67.11 66.60 70.56 54.83 80.74 86.63 72.50 86.22 71.98 82.20 74.63 83.81 83.30	69.37 68.77 68.13 71.94 71.60 73.15 54.83 86.59 90.21 85.48 90.38 76.12 88.47 79.47 88.62 88.93	72.73 69.10 71.98 71.75 75.30 77.25 70.81 54.83 89.62 91.50 91.65 92.96 82.56 91.14 90.69 89.98	76.57 70.19 73.53 78.78 79.47 81.10 56.08 92.15 94.98 95.89 95.25 84.17 94.37 89.53 93.51	78.89 71.68 74.87 81.46 83.57 84.98 56.50 93.68 96.18 97.36 96.44 87.64 96.10 92.90 94.87
Co	oCoOp gCoOp gCoOp oGrad aPLe LIP-SVD (Ours) IP LIP-Adapter p-Adapter-F near Probing P++ oOp oCoOp gCoOp gCoOp oGrad aPLe	67.92 67.03 67.11 66.60 70.56 54.83 80.74 86.63 72.50 86.22 71.98 82.20 74.63 83.81 83.30	68.77 68.13 71.94 71.60 73.15 54.83 86.59 90.21 85.48 90.38 76.12 88.47 79.47 88.62 88.93	69.10 71.98 71.75 75.30 77.25 70.81 54.83 89.62 91.50 91.65 92.96 82.56 91.14 90.69 89.98	70.19 73.53 78.78 79.47 81.10 56.08 92.15 94.98 95.89 95.25 84.17 94.37 89.53 93.51	71.68 74.87 81.46 83.57 84.98 56.50 93.68 96.18 97.36 96.44 87.64 96.10 92.90 94.87
Kg Pro Ma	gCoOp oGrad aPLe LIP-SVD (Ours) LIP LIP-Adapter p-Adapter-F near Probing P++ oOp oCoOp gCoOp gCoOp oGrad aPLe	67.03 67.11 66.60 70.56 54.83 80.74 86.63 72.50 86.22 71.98 82.20 74.63 83.81 83.30	68.13 71.94 71.60 73.15 54.83 86.59 90.21 85.48 90.38 76.12 88.47 79.47 88.62 88.93	71.98 71.75 75.30 77.25 70.81 54.83 89.62 91.50 91.65 92.96 82.56 91.14 90.69 89.98	73.53 78.78 79.47 81.10 56.08 92.15 94.98 95.89 95.25 84.17 94.37 89.53 93.51	74.87 81.46 83.57 84.98 56.50 93.68 96.18 97.36 96.44 87.64 96.10 92.90 94.87
Flowers 102 Co Co Co Kg Pro Ma CI CI Ti Ti Li Li Co Co Kg Pro Pro	oGrad aPLe LIP-SVD (Ours) LIP LIP-Adapter p-Adapter-F near Probing 0-++ 0Op 0CoOp gCoOp gCoOp oGrad aPLe	67.11 66.60 70.56 54.83 80.74 86.63 72.50 86.22 71.98 82.20 74.63 83.81 83.30	71.94 71.60 73.15 54.83 86.59 90.21 85.48 90.38 76.12 88.47 79.47 88.62 88.93	71.75 75.30 77.25 70.81 54.83 89.62 91.50 91.65 92.96 82.56 91.14 90.69 89.98	78.78 79.47 81.10 56.08 92.15 94.98 95.89 95.25 84.17 94.37 89.53 93.51	81.46 83.57 84.98 56.50 93.68 96.18 97.36 96.44 87.64 96.10 92.90 94.87
Mac CL	aPLe LIP-SVD (Ours) LIP LIP-Adapter p-Adapter-F near Probing P++ DOP DCOOP gCOOP gCOOP oGrad aPLe	54.83 80.74 86.63 72.50 86.22 71.98 82.20 74.63 83.81 83.30	71.60 73.15 54.83 86.59 90.21 85.48 90.38 76.12 88.47 79.47 88.62 88.93	75.30 77.25 70.81 54.83 89.62 91.50 91.65 92.96 82.56 91.14 90.69 89.98	79.47 81.10 56.08 92.15 94.98 95.89 95.25 84.17 94.37 89.53 93.51	83.57 84.98 56.50 93.68 96.18 97.36 96.44 87.64 96.10 92.90 94.87
CL CL Tiq Tiq Lin Lin Cl Cl Cl Cl Cl Cl Cl C	LIP-SVD (Ours) LIP LIP-Adapter p-Adapter p-Adapter-F near Probing P++ DOP DCOOP gCoOp gCoOp oGrad aPLe	70.56 54.83 80.74 86.63 72.50 86.22 71.98 82.20 74.63 83.81 83.30	73.15 54.83 86.59 90.21 85.48 90.38 76.12 88.47 79.47 88.62 88.93	77.25 70.81 54.83 89.62 91.50 91.65 92.96 82.56 91.14 90.69 89.98	56.08 92.15 94.98 95.89 95.25 84.17 94.37 89.53 93.51	56.50 93.68 96.18 97.36 96.44 87.64 96.10 92.90 94.87
CL CI Tip Tip Lip Co Co Co CI Tip CI CI CI CI CI CI CI C	LIP LIP-Adapter p-Adapter p-Adapter-F near Probing P++ OOp pCoOp gCoOp gCoOp oGrad aPLe	54.83 80.74 86.63 72.50 86.22 71.98 82.20 74.63 83.81 83.30	54.83 86.59 90.21 85.48 90.38 76.12 88.47 79.47 88.62 88.93	70.81 54.83 89.62 91.50 91.65 92.96 82.56 91.14 90.69 89.98	56.08 92.15 94.98 95.89 95.25 84.17 94.37 89.53 93.51	56.50 93.68 96.18 97.36 96.44 87.64 96.10 92.90 94.87
Flowers 102 Flowers 102 Flowers 102 Flowers 102 Flowers 102 Co Kg Pro Mi CU CU Tip Tip Lin FGVCAircraft FGVCAircraft CL Co Kg Pro Co Co Kg Pro Pro Co Co Kg Pro Pro Pro Pro Pro Pro Pro Pr	JIP-Adapter p-Adapter p-Adapter-F near Probing P++ OOp pCoOp gCoOp gGrad aPLe	80.74 86.63 72.50 86.22 71.98 82.20 74.63 83.81 83.30	86.59 90.21 85.48 90.38 76.12 88.47 79.47 88.62 88.93	54.83 89.62 91.50 91.65 92.96 82.56 91.14 90.69 89.98	92.15 94.98 95.89 95.25 84.17 94.37 89.53 93.51	93.68 96.18 97.36 96.44 87.64 96.10 92.90 94.87
Flowers 102 Flowe	p-Adapter p-Adapter-F mear Probing P++ pOp pCoOp gCoOp gGrad aPLe	80.74 86.63 72.50 86.22 71.98 82.20 74.63 83.81 83.30	86.59 90.21 85.48 90.38 76.12 88.47 79.47 88.62 88.93	89.62 91.50 91.65 92.96 82.56 91.14 90.69 89.98	92.15 94.98 95.89 95.25 84.17 94.37 89.53 93.51	93.68 96.18 97.36 96.44 87.64 96.10 92.90 94.87
Flowers 102	p-Adapter-F near Probing P++ OPp OCOOp gCoOp oGrad aPLe	86.63 72.50 86.22 71.98 82.20 74.63 83.81 83.30	90.21 85.48 90.38 76.12 88.47 79.47 88.62 88.93	91.50 91.65 92.96 82.56 91.14 90.69 89.98	94.98 95.89 95.25 84.17 94.37 89.53 93.51	96.18 97.36 96.44 87.64 96.10 92.90 94.87
Flowers 102	p-Adapter-F near Probing P++ OPp OCOOp gCoOp oGrad aPLe	86.63 72.50 86.22 71.98 82.20 74.63 83.81 83.30	85.48 90.38 76.12 88.47 79.47 88.62 88.93	91.65 92.96 82.56 91.14 90.69 89.98	95.89 95.25 84.17 94.37 89.53 93.51	97.36 96.44 87.64 96.10 92.90 94.87
Flowers 102 Flowers 102 Lin Co Co Kg Pro Mia CI CI Tip Tip Lin Lin Co Co Kg Pro	near Probing P++ Op CoOp gCoOp gGrad aPLe	86.22 71.98 82.20 74.63 83.81 83.30	90.38 76.12 88.47 79.47 88.62 88.93	92.96 82.56 91.14 90.69 89.98	95.25 84.17 94.37 89.53 93.51	96.44 87.64 96.10 92.90 94.87
Flowers 102	P++ OOp OCoOp gCoOp oGrad aPLe	86.22 71.98 82.20 74.63 83.81 83.30	90.38 76.12 88.47 79.47 88.62 88.93	92.96 82.56 91.14 90.69 89.98	95.25 84.17 94.37 89.53 93.51	96.44 87.64 96.10 92.90 94.87
Flowers 102 Co	oOp oCoOp gCoOp oGrad aPLe	71.98 82.20 74.63 83.81 83.30	76.12 88.47 79.47 88.62 88.93	82.56 91.14 90.69 89.98	84.17 94.37 89.53 93.51	87.64 96.10 92.90 94.87
FGVCAircraft Co Co Kg Pro Ma CI CI Tip Lin Lin Co Co Kg Pro Pro Rg Pro Rg	oCoOp gCoOp oGrad aPLe	82.20 74.63 83.81 83.30	88.47 79.47 88.62 88.93	91.14 90.69 89.98	94.37 89.53 93.51	96.10 92.90 94.87
FGVCAircraft Kg Pro Ma CI CI Til Til Lin Lin Kg Co Co Kg Pro Pro	gCoOp oGrad aPLe	74.63 83.81 83.30	79.47 88.62 88.93	90.69 89.98	89.53 93.51	92.90 94.87
FGVCAircraft FGVCAircraft FGVCAircraft FGVCAircraft FGVCAircraft FGVCAircraft FGVCAircraft FGVCAircraft	oGrad aPLe	83.81 83.30	88.62 88.93	89.98	93.51	94.87
FGVCAircraft MacCL CL Tip Lin Lin Co Co Kg Pro	aPLe	83.30	88.93			
CL CL Tip Tip Lin Lin FGVCAircraft Co Co Kg Pro				02.01	30.00	
CL Tip Tip Lin FGVCAircraft FGVCAircraft Co Co Kg Pro			90.32	93.44	95.49	97.50
CL Tip Tip Lin FGVCAircraft FGVCAircraft Co Co Kg Pro	JP			24.81		
Tip Tip Tip Lin	LIP-Adapter	27.60	29.60	31.10	37.20	42.67
FGVCAircraft LP Co Co Kg Pro	p-Adapter	27.22	28.08	30.19	34.12	37.64
FGVCAircraft LP Co Co Kg Pro	p-Adapter-F	29.58	32.51	35.15	40.61	45.59
FGVCAircraft LP Co Co Kg Pro	near Probing	20.13	23.78	29.46	37.18	42.85
FGVCAircraft Co Co Kg Pro	_	29.11	32.32	34.31	38.83	41.46
Co Kg Pro		15.03	26.53	26.73	33.18	40.93
Kg Pro	СоОр	13.20	30.87	31.29	29.57	37.63
Pro	gCoOp	26.90	28.07	32.47	34.97	36.27
	oGrad	27.97	30.84	32.93	37.89	40.39
1V14	aPLe	26.73	30.90	34.87	42.00	48.40
	LIP-SVD (Ours)	31.11	34.85	39.42	45.91	52.49
	LIP			62.60		
	LIP-Adapter	67.10	69.00	71.30	73.13	75.30
	p-Adapter	65.37	66.46	68.39	70.13	75.30
	p-Adapter-F	64.49	66.74	70.29	73.60	74.99
	near Probing	39.83	52.70	63.07	69.54	73.29
	near Probing P++		52.70 70.09	73.22	$\frac{69.54}{75.14}$	76.09
SUN397		67.56 64.70		73.22	$75.14 \\ 72.50$	76.09
	Op		66.40			
	CoOp	68.19	69.11	70.50	70.62	72.05
	gCoOp	68.43	69.53	71.79	72.50	73.40
	oGrad	64.54	68.51	71.17	72.91	75.00
Ma CL	DI	64.77 70.37	67.10 71.93	70.67 73.75	73.23 75.16	75.53 76.85

Table S12 (continued): **Natural per-dataset performance** comparison of with various methods in few-shot setting in terms of classification accuracy (%).

Dataset	Method	K = 1	K = 2	K = 4	K = 8	K = 16
	CLIP	<u> </u> 		89.10		
	CLIP-Adapter	89.03	89.73	90.87	91.77	92.03
	Tip-Adapter	89.32	88.52	89.36	90.69	92.03 91.32
					92.09	92.70
	Tip-Adapter-F Linear Probing	90.72	91.10	91.58		
	C	40.70	55.03	69.96	79.99	85.80
OxfordPets	LP++	89.52	89.94	91.09	91.91	92.80
	CoOp	92.20	89.20	91.30	90.83	91.80
	CoCoOp	91.17	92.14	93.01	93.44	93.25
	KgCoOp	91.97	92.13	93.20	93.10	93.23
	ProGrad	89.01	90.55	93.21	92.18	92.13
	MaPLe	89.10	90.87	91.90	92.57	92.83
	CLIP-SVD (Ours)	92.67	92.09	92.83	92.57	93.77
	CLIP			67.64		
	CLIP-Adapter	69.67	74.10	77.30	81.87	84.53
	Tip-Adapter	68.92	71.50	74.07	75.65	77.35
	Tip-Adapter-F	73.27	76.11	80.24	82.24	84.50
	Linear Probing	48.24	61.08	70.87	77.51	81.27
LICEIOI	LP++	72.36	75.13	79.49	82.17	83.75
UCF101	СоОр	24.96	25.89	23.85	26.23	28.48
	СоСоОр	25.42	28.85	30.66	21.78	24.86
	KgCoOp	72.93	74.83	78.40	80.03	81.43
	ProGrad	71.91	74.39	77.82	88.64	81.59
	MaPLe	71.83	74.60	78.47	81.37	85.03
	CLIP-SVD (Ours)	76.34	79.69	81.80	83.95	86.58
	CLIP	 		85.87		
	CLIP-Adapter	85.90	86.10	86.47	86.67	86.83
	Tip-Adapter	85.14	86.03	85.99	86.42	86.36
	Tip-Adapter-F	86.01	86.26	86.48	86.74	87.24
	Linear Probing	44.63	62.66	72.96	78.98	83.69
	LP++	83.23	86.12	85.94	86.76	87.28
Food101	СоОр	82.07	80.80	82.58	83.37	85.17
	CoCoOp	86.10	86.21	86.64	86.92	87.19
	KgCoOp	86.27	86.60	86.59	86.90	87.03
	ProGrad	82.75	84.81	85.77	85.91	87.01
	MaPLe	80.50	81.47	81.77	83.60	85.33
	CLIP-SVD (Ours)	85.82	85.58	85.47	85.59	86.00
		1 00.02	00.00		00.00	
	CLIP	67.97	70.00	65.36	76.00	70.00
	CLIP-Adapter	67.87	70.20	72.65	76.92	79.86
	Tip-Adapter	68.89	70.42	72.69	74.41	76.44
	Tip-Adapter-F	70.62	73.08	75.75	78.51	81.15
	Linear Probing	45.77	56.92	66.79	73.43	78.39
Average	LP++	70.35	72.93	75.77	77.94	80.32
5	CoOp	68.09	70.13	73.59	76.45	79.01
	CoCoOp	66.95	67.63	71.98	72.92	75.02
	KgCoOp	69.51	71.57	74.48	75.82	77.26
	ProGrad	68.20	71.78	74.21	77.93	79.20
	MaPLe	69.27	72.58	75.37	78.89	81.79
	CLIP-SVD (Ours)	73.20	76.06	78.18	80.55	82.97

Table S13: **Biomedical per-dataset performance** comparison of CLIP-SVD with various methods in few-shot setting in terms of classification accuracy (%).

Dataset	Method	K = 1	K = 2	K = 4	K = 8	K = 16
	BiomedCLIP			56.79		
	CLIP-Adapter	56.80	57.13	56.80	57.15	60.16
	Tip-Adapter	66.66	67.77	76.37	73.75	78.97
	Tip-Adapter-F	59.60	61.94	77.90	79.18	82.27
	Standard LP	62.24	72.45	75.98	77.63	81.24
DED (D)	LP++	64.72	71.69	75.48	77.11	81.61
BTMRI	CoOp	63.82	68.82	74.68	79.27	82.37
	CoCoOp	59.47	64.14	67.83	71.69	78.45
	KgCoOp	63.33	70.16	75.40	79.79	81.07
	ProGrad	66.92	71.46	76.24	78.82	82.84
	MaPLe	38.01	37.02	42.36	50.75	56.22
	BiomedCoOp	65.08	70.57	77.23	78.55	83.30
	CLIP-SVD (Ours)	63.25	73.62	78.43	83.21	84.64
	BiomedCLIP	1		59.75		
	CLIP-Adapter	61.44	61.01	61.72	61.86	63.55
	Tip-Adapter	62.71	61.44	59.03	55.93	68.78
	Tip-Adapter-F	61.86	56.35	64.54	68.50	71.89
	Standard LP	51.41	47.88	53.38	65.53	68.78
DIICI	LP++	51.12	55.50	60.31	66.10	70.05
BUSI	СоОр	48.73	53.53	60.17	64.69	69.49
	CoCoOp	52.26	49.15	59.75	65.82	70.2
	KgCoOp	53.39	55.51	62.01	67.37	70.62
	ProGrad	46.33	49.15	62.29	64.83	71.47
	MaPLe	41.38	33.47	47.74	42.65	45.62
	BiomedCoOp	50.71	50.71	59.32	63.27	70.34
	CLIP-SVD (Ours)	61.58	63.56	68.12	73.87	74.29
	BiomedCLIP			43.8		
	CLIP-Adapter	50.42	43.04	46.28	48.68	49.55
	Tip-Adapter	62.13	58.72	63.84	66.77	73.05
	Tip-Adapter-F	54.89	54.01	69.97	69.89	76.07
	Standard LP	49.91	48.06	60.55	68.29	71.98
COVID OILE	LP++	46.41	56.42	62.32	66.19	72.79
COVID-QU-Ex	СоОр	58.82	58.37	67.03	74.66	76.37
	CoCoOp	69.36	68.80	63.70	69.36	74.52
	KgCoOp	61.68	54.68	65.91	74.86	75.65
	ProGrad	60.42	64.22	68.56	74.65	74.93
	MaPLe	35.86	38.99	33.32	36.43	40.89
	BiomedCoOp	72.64	71.53	73.28	76.26	78.72
	CLIP-SVD (Ours)	71.15	71.08	70.47	73.97	73.14
	BiomedCLIP			42.43		
	CLIP-Adapter	47.17	41.94	42.19	44.64	47.28
	Tip-Adapter	45.85	51.65	55.33	69.89	73.38
	Tip-Adapter-F	46.68	58.99	60.18	75.24	82.07
	Standard LP	43.82	59.35	69.54	78.89	82.50
CELLIDATEM	LP++	57.70	61.57	65.73	77.06	79.07
CTKIDNEY	СоОр	54.51	60.57	68.12	77.40	83.52
	CoCoOp	47.88	52.71	61.07	73.93	77.70
	KgCoOp	58.92	62.81	68.68	77.43	77.67
	ProGrad	54.65	64.66	67.90	78.23	81.13
	MaPLe	30.62	38.98	38.00	39.67	51.06
	BiomedCoOp	56.13	64.21	66.50	77.16	83.20

Table S13 (continued): **Biomedical per-dataset performance** comparison of CLIP-SVD with various methods in few-shot setting in terms of classification accuracy (%).

Dataset	Method	K = 1	K = 2	K = 4	K = 8	K = 16
	BiomedCLIP	1		54.58		
	CLIP-Adapter	54.83	54.83	54.83	56.08	56.50
	Tip-Adapter	56.72	60.94	69.61	69.13	74.22
	Tip-Adapter-F	59.19	64.22	69.94	75.86	78.00
	Standard LP	54.30	62.00	72.38	78.88	79.00
Kvasir	LP++	58.27	60.47	69.36	72.52	75.41
	CoOp	58.2	64.86	70.78	77.14	77.88
	CoCoOp	59.45	65.50	68.94	72.92	75.22
	KgCoOp	61.67	65.67	68.28	72.05	72.95
	ProGrad	60.78	64.70	70.00	76.03	75.88
	MaPLe	41.06	45.17	53.22	56.03	63.50
	BiomedCoOp	62.17	67.25	74.08	77.72	78.89
	CLIP-SVD (Ours)	65.08	72.08	74.92	80.08	82.83
	BiomedCLIP			30.65		
	CLIP-Adapter	31.27	31.67	33.26	36.48	42.06
	Tip-Adapter	46.14	63.32	70.05	69.57	77.68
	Tip-Adapter-F	52.81	58.90	71.74	74.51	80.43
	Standard LP	58.44	64.42	71.07	76.30	80.34
CHANICT	LP++	57.18	60.61	67.79	72.40	78.32
CHMNIST	CoOp	57.34	59.68	68.66	75.00	79.63
	CoCoOp	49.07	50.82	58.58	66.58	72.16
	KgCoOp	59.02	60.06	68.77	69.50	73.58
	ProGrad	60.15	59.60	69.13	70.99	75.11
	MaPLe	48.05	57.76	65.87	68.88	71.99
	BiomedCoOp	59.82	59.79	71.19	74.78	79.05
	CLIP-SVD (Ours)	54.94	66.13	75.69	81.05	84.75
	BiomedCLIP			50.03		
	CLIP-Adapter	54.83	53.47	52.91	56.33	57.56
	Tip-Adapter	75.37	72.73	83.32	87.25	89.17
	Tip-Adapter-F	74.21	71.82	79.57	90.41	92.35
	Standard LP	74.50	78.40	85.30	90.24	92.77
I C25000	LP++	63.05	71.42	82.61	89.14	92.58
LC25000	CoOp	71.90	76.55	84.66	87.50	92.19
	CoCoOp	63.66	71.76	77.44	85.57	87.38
	KgCoOp	71.80	75.18	82.10	84.63	86.79
	ProGrad	72.48	74.76	84.72	87.86	90.70
	MaPLe	67.13	69.80	76.73	82.19	86.73
	BiomedCoOp	77.56	77.74	85.60	88.77	92.68
	CLIP-SVD (Ours)	72.34	82.31	89.01	89.98	91.52
	BiomedCLIP			26.26		
	CLIP-Adapter	25.49	25.49	26.07	25.84	26.05
	Tip-Adapter	26.52	31.07	43.42	48.08	54.23
	Tip-Adapter-F	39.53	33.07	47.37	56.07	62.85
	Standard LP	39.35	46.03	51.31	53.94	62.27
DETENIA	LP++	35.77	39.37	46.95	53.44	60.62
RETINA	СоОр	35.02	35.26	42.22	51.87	59.38
	СоСоОр	32.94	36.43	39.75	48.45	53.91
	KgCoOp	33.54	35.17	42.61	49.97	51.18
	ProGrad	33.49	36.49	43.09	52.26	50.47
	MaPLe	27.73	31.07	30.89	41.80	53.78
	BiomedCoOp	36.64	38.67	45.58	56.47	61.28

Table S13 (continued): **Biomedical per-dataset performance** comparison of CLIP-SVD with various methods in few-shot setting in terms of classification accuracy (%).

Dataset	Method	K = 1	K = 2	K = 4	K = 8	K = 16
	BiomedCLIP			29.53		
	CLIP-Adapter	29.00	28.66	28.96	28.80	29.08
	Tip-Adapter	29.04	33.55	24.19	25.76	33.17
	Tip-Adapter-F	30.01	28.38	26.59	26.46	27.67
	Standard LP	26.02	26.57	27.83	22.20	23.97
KneeXray	LP++	21.25	26.40	28.92	23.75	26.38
KileeAlay	CoOp	24.96	25.89	23.85	26.23	28.48
	CoCoOp	25.42	28.85	30.66	21.78	24.86
	KgCoOp	29.07	28.14	22.44	23.37	24.80
	ProGrad	30.09	23.83	23.95	24.78	26.27
	MaPLe	23.41	22.67	22.56	24.78	25.87
	BiomedCoOp	36.13	37.72	35.91	37.7	39.69
	CLIP-SVD (Ours)	27.38	27.05	27.67	30.70	38.37
	BiomedCLIP			30.00		
	CLIP-Adapter	44.00	49.73	49.96	49.50	52.73
	Tip-Adapter	32.36	33.8	38.10	53.93	53.33
	Tip-Adapter-F	46.66	53.93	55.20	65.00	72.50
	Standard LP	47.25	54.21	61.00	65.85	69.40
OCTMNIST	LP++	47.24	53.18	59.02	63.69	68.35
OCTAINIST	CoOp	52.63	53.57	53.37	63.67	65.47
	CoCoOp	49.33	50.93	48.57	55.40	60.67
	KgCoOp	50.63	50.53	52.97	61.03	62.80
	ProGrad	51.40	55.33	55.07	62.17	63.33
	MaPLe	26.63	34.00	30.17	30.53	33.63
	BiomedCoOp	51.83	55.03	54.73	58.87	66.93
	CLIP-SVD (Ours)	50.63	66.67	68.97	79.07	80.67
	BiomedCLIP			42.38		
	CLIP-Adapter	45.53	44.70	45.30	46.54	48.46
	Tip-Adapter	50.35	53.50	58.33	62.01	67.60
	Tip-Adapter-F	52.55	54.17	62.30	68.12	68.12
	Standard LP	48.91	55.82	62.12	67.33	70.81
Average	LP++	49.27	55.88	61.30	65.48	70.09
Average	CoOp	52.59	55.71	61.35	67.74	71.48
	CoCoOp	50.88	53.91	57.63	63.15	67.51
	KgCoOp	54.31	55.79	60.92	66.00	67.71
	ProGrad	53.67	56.42	62.10	67.06	69.21
	MaPLe	37.99	40.89	44.09	47.37	52.93
	BiomedCoOp	56.87	59.32	64.34	68.96	73.41
	CLIP-SVD (Ours)	56.35	62.63	68.02	73.26	76.46

Table S14: Natural Base-to-novel generalization comparison of CLIP-SVD with previous methods

Dataset		CLIP			•		-	CLIP-SVD
		[57]	[82]	[81]	[71]	[84]	[35]	(Ours)
Average on	Base	69.34	82.69	80.47	80.73	82.48	82.28	84.38
Average on 11 datasets	Novel	74.22	63.22	71.69	73.60	70.75	75.14	76.29
11 datasets	HM	71.70	71.66	75.83	77.00	76.16	78.55	80.13
	Base	72.43	76.47	75.98	75.83	77.02	76.66	78.01
ImageNet	Novel	68.14	67.88	70.43	69.96	66.66	70.54	70.71
	HM	70.22	71.92	73.10	72.78	71.46	73.47	74.18
	Base	96.84	98.00	97.96	97.72	98.02	97.74	$\boldsymbol{98.54}$
Caltech101	Novel	94.00	89.81	93.81	94.39	93.89	94.36	94.00
	HM	95.40	93.73	95.84	96.03	95.91	96.02	96.21
	Base	91.17	93.67	95.20	94.65	95.07	95.43	96.28
OxfordPets	Novel	97.26	95.29	97.69	97.77	97.63	97.76	97.60
	HM	94.12	94.47	96.43	96.18	96.33	96.58	96.93
Stanford	Base	63.37	78.12	70.49	71.76	77.68	72.94	78.89
Cars	Novel	74.89	60.40	73.59	75.04	68.63	74.00	74.03
	HM	68.65	68.13	72.01	73.36	72.88	73.47	76.38
	Base	72.08	97.60	94.87	95.00	95.54	95.92	96.30
Flowers 102	Novel	77.80	59.67	71.75	74.73	71.87	72.46	76.19
	HM	74.83	74.06	81.71	83.65	82.03	82.56	85.07
	Base	90.10	88.33	90.70	90.50	90.37	90.71	90.52
Food101	Novel	91.22	82.26	91.29	91.70	89.59	92.05	91.74
	HM	90.66	85.19	90.99	91.09	89.98	91.38	91.13
FGVC	Base	27.19	40.44	33.41	36.21	40.54	37.44	44.00
Aircraft	Novel	36.29	22.30	23.71	33.55	27.57	35.61	37.01
	HM	31.09	28.75	27.74	34.83	32.82	36.50	40.20
	Base	69.36	80.60	79.74	80.29	81.26	80.82	$\bf 82.56$
SUN397	Novel	75.35	65.89	76.86	76.53	74.17	78.70	78.98
	HM	72.23	72.51	78.27	78.36	77.55	79.75	80.73
	Base	53.24	79.44	77.01	77.55	77.35	80.36	82.91
DTD	Novel		41.18	56.00	54.99	52.35	59.18	65.42
	HM	56.37	54.24	64.85	64.35	62.45	68.16	73.13
EuroSAT	Base	56.48	92.19	87.49	85.64	90.11	94.07	94.53
	Novel		54.74	60.04	64.34	60.89	73.23	74.03
	HM	60.03	68.69	71.21	73.48	72.67	82.35	83.03
	Base	70.53	84.69	82.33	82.89	84.33	83.00	85.66
UCF101	Novel		56.05	73.45	76.67	74.94	78.66	79.45
	HM	73.85	67.46	77.64	79.65	79.35	80.77	82.44

 $\hbox{ Table S15: } \textbf{Biomedical Base-to-novel generalization} \ \ \text{comparison of CLIP-SVD} \ \ \text{with previous methods}$

Dataset		CLIP	_	_				BiomedCoOp	
		[57]	[82]	[81]	[71]	[84]	[35]	[39]	(Ours)
Average on 9 datasets	Base	49.27	76.71	75.52	71.90	75.69	65.40	78.60	82.64
	Novel	67.17	65.34	67.74	65.94	67.33	49.51	73.90	74.31
	HM	55.23	68.80	69.11	67.22	69.86	53.10	74.04	78.25
	Base	40.88	82.25	77.88	78.00	82.13	66.17	82.42	88.83
BTMRI	Novel	96.18	94.51	94.84	95.05	94.98	49.58	96.84	94.98
	HM	57.37	87.95	85.53	85.69	88.09	56.69	89.05	91.80
	Base	53.96	75.92	77.28	75.42	75.19	61.36	75.91	75.39
COVID-QU-Ex	Novel	89.43	90.07	87.61	89.61	90.34	71.25	91.63	89.56
	HM	67.31	82.39	82.12	81.90	82.07	65.94	83.03	81.87
	Base	38.55	82.24	81.96	81.67	83.86	63.99	86.93	88.31
CTKIDNEY	Novel	52.99	67.92	56.56	58.45	63.01	63.51	78.94	68.02
	HM	44.63	74.40	66.93	68.14	71.96	63.75	$\bf 82.74$	76.85
	Base	75.00	86.22	85.94	81.56	82.89	76.66	86.50	86.78
Kvasir	Novel	60.50	58.06	53.95	59.00	60.45	26.17	61.83	61.89
	HM	66.97	69.39	66.29	68.47	69.91	39.02	72.11	72.25
	Base	37.63	89.41	87.77	75.45	82.98	89.19	88.87	90.38
CHMNIST	Novel	40.69	35.11	42.51	38.70	44.19	23.76	42.73	35.42
	HM	39.10	50.42	57.28	51.16	57.67	37.52	57.71	50.89
	Base	59.73	90.12	88.33	88.13	90.29	87.16	93.77	96.68
LC25000	Novel	87.60	87.55	95.02	86.44	85.47	52.66	97.00	96.36
	HM	71.03	88.82	91.55	87.28	87.81	65.65	95.36	$\boldsymbol{96.52}$
	Base	45.18	70.98	66.88	60.77	68.77	57.40	68.46	84.62
RETINA	Novel	55.28	56.90	65.56	54.91	58.43	53.33	67.72	84.88
	HM	49.72	63.16	66.21	57.69	63.18	55.29	68.09	84.75
	Base	35.89	38.28	34.08	37.94	40.88	36.44	44.23	43.73
KneeXray	Novel	71.90	47.69	63.14	61.19	59.12	55.35	78.35	76.52
	HM	47.88	42.47	44.27	46.84	48.34	43.95	$\boldsymbol{56.54}$	55.65
	Base	56.60	75.00	79.60	68.20	74.20	50.27	80.33	89.00
OCTMNIST	Novel	50.00	50.23	50.47	50.13	50.02	50.00	50.07	61.13
	HM	53.10	60.17	61.77	57.79	59.76	50.13	61.69	72.48